Responses to Reviewers' Comments

We really appreciate the efforts made by the reviewers to help us improve this paper. The insightful comments and questions raised by the reviewers gave us a chance to look more deeply into the problems we are trying to tackle. Understanding that the main concerns are concentrated on the performance of DT-SDH under skewed datasets, we dedicated most of our efforts to improving our reasoning and writing related to this problem in preparing an updated draft of this paper. In the following text, we first describe in general the changes made in the new draft, and then respond to individual comments.

G1. We reorganized and enhanced our elaborations about skewed datasets, focusing on Section 6.1.3. The main information we are trying to convey is: 1) tight clusters can change the running time and even the time complexity of the algorithm; 2) in most cases tight clusters have positive impact by decreasing the running time; and 3) the clusters have to be placed in a certain way to have a negative impact on the running time. We will have more discussions on this in our responses to individual comments;

G2. We performed additional experiments to verify our claims made in item G1 (also to respond to reviewers' requests). For such experiments, we generate input data with different levels of "skewness" using high-order Zipf and mixed Gaussian models. The results show that data skewness generally improves running time of the algorithm. Such results can be found in Section 7.4.

G3. Various editorial efforts were made to improve the readability of the whole paper. We also removed the section about approximate algorithms (previously Section 7) since we believe it serves more like a motivation of this analytical work and thus is not worth a length coverage. The excessive length of the paper is another concern.

0.1 Reviewer 1

R1-1. *Now, I cannot believe that this would fix the skewness problem. Consider a quadtree, where there are n 2D points. Suppose at every level, three of the leaf nodes just contain one point each while the fourth leaf node contains $n-3$ points. Such a quadtree will be of O(n) depth. Even worse, suppose there are $\beta+1$ points so tightly clumped up (called "tight clumps") together such that every subdivision creates three empty leaf nodes and one leaf node containing all the $\beta+1$ points, in which case the depth of the quadtree can be very large.*

Response: First we admit that our description about the tree height H was not very clear and we apologize for the confusion. In this draft, we have fixed it by using Eq. (1) to define it explicitly. Note that H is of $O(\log N)$ and is not related to data distribution. A path from the root to any leaf node will have at most H depth. Even in the special case presented by the reviewer, the tree height will never reach $O(N)$. Instead, space partition will stop after H levels - this means that, in the aforementioned case, there will be one node with $O(N)$ points and many nodes that are empty or nearly empty. The empty nodes are easily ignored by our algorithm and will thus decrease the running time. Considering the trimmed empty nodes, we admit that it is not rigorous to say the tree is "balanced". However, we believe the performance of the algorithm will not suffer from such imbalance. We will elaborate more in our responses to comment R1-2.

Now, I don't quite understand what the authors mean by "the average number of points in the leaf nodes is no smaller than a predefined threshold β". I think what the authors are saying is that they stop subdividing when the "average" number of points averaged across all the leaf nodes in a level is "no smaller" (should be smaller, no?) than β.

Response: For the purpose of setting a cap of the tree height, we want each leaf node, on average, to contain *at least* β points. Therefore, it is correct to say "no smaller than" here. Setting this threshold to a fixed β is essential in that we know when N increases to $s^d N$, the height of the tree increases by 1.

R1-2. *In that case, you can have a case that one leaf node contains $O(n)$ points and others are largely empty? How does this affect the algorithm?*

Response: Indeed, one node can have $O(N)$ points. We depicted this scenario in Fig. 1 in the next page, in which the filled square A represents the node where most of the data points are located, and the rest of the points are distributed sporadically out of A. In this case, the point-to-point distances can be divided into two categories: (1) distances for which two points are both in A (named *internal* distance); and (2) distances between one point in A and one out of A (named *external* distance). We can easily see that a majority of the distances are internal. Running DT-SDH to process the above dataset, we have the following observations:

(1) As compared to a uniform dataset, we can quickly reach the level of density map where A is located

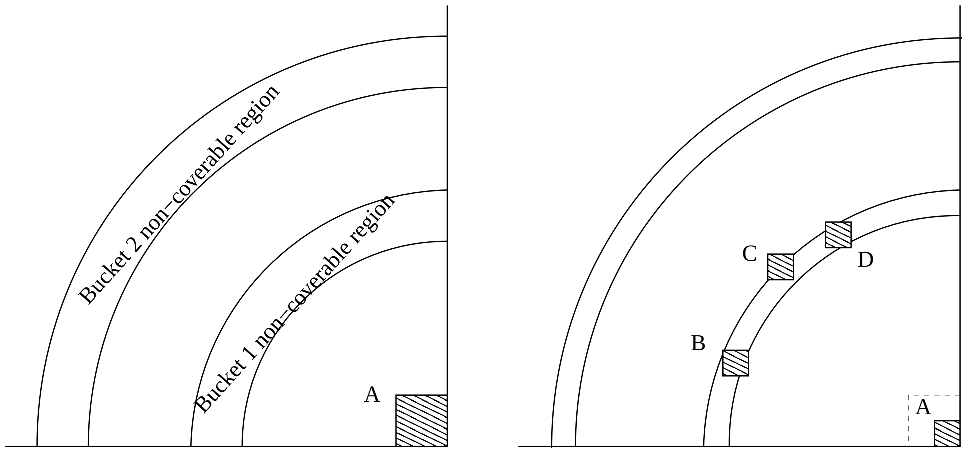

Fig. 1 An extreme case of skewed 2D dataset. The partial annuli (i.e., rings) represent non-coverable regions after visiting the lowest level tree nodes. The left figure shows the situation of a dataset with size N and the right figure when the data size increases to $4N$. Only one corner of the simulation space is illustrated.

to resolve cell pairs. This is because most of the nodes are empty and thus skipped by DT-SDH, thus decreasing the number of type (i) operations mentioned in Section 3.1;

(2) The internal distances can be resolved into bucket $[0, p)$ in one shot; and

(3) As compared to a uniform dataset, it is possible that more time will be spent to resolve cell pairs to handle the external distances. However, to make a bad case out of this, we have to put most points out of A into the non-coverable regions (e.g., partial rings in Fig. 1). For example, clusters B, C, and D in the right graph of Fig. 1 are non-resolvable with A. Otherwise, the number of non-resolved external distances will follow Theorem 3.

From the above observations, we can see that the aforementioned dataset makes a particularly “good” case for our algorithm. Here we want to emphasize observation (3), which shows that it takes some extra efforts and bizarre data placement to create a “bad” case.

In summary, the impact of tight clusters is two-fold: first, they tend to decrease the running time according to observations (1) and (2); on the other hand, if clusters are placed properly, the running time can be elongated (observation (3)). Only when the latter impact overshadows the benefits caused by the former one, we have a “bad” case for which the running time (or even time complexity) can increase. In fact, our experimental results in Section 7.4 show that the benefits of tight clusters dominate in most of the cases. Among the tens of skewed data patterns we tested, only one turned out to be a “bad” distribution.

Against observation (1), one might argue that, if the clumps are of sizes larger than p, the internal distances cannot be immediately resolved into the first bucket of SDH. We also did some research on this scenario and have the following findings. The distribution of the internal distances within a closed region (e.g., a clump of points) has one single peak, as shown in Fig. 13 (middle graph) of the paper. Depending on the size and shape of the clump, the peak can appear anywhere from 0 to the maximum distance within the clump. According to the discussions related to Fig. 13, the performance of DT-SDH degrades only when the peak of the density function is close to the boundary of two buckets. Let us call the above observation (4). Similar to observation (3), it shows that only clumps with specific features render a “bad” case for DT-SDH.

R1-3. *Now, it seems to be the “rare counter example to Theorem 3” is related to the skewness in the tree I refer above. The authors refer to the case when the points are clumped up near bucket (histogram) boundaries, the number of unresolvable distances becomes large. This is understandable but here I don’t agree with the way the authors have portrayed the problem. The authors seem to portray that the worse case only happens when if clumping happens at specific places. I think the problem is more common than that. I think clumping of points, if happens, is sufficient for the worse case to happen. Here is my reasoning for it.*

Say, we have a dataset with lots of clumps. I think that regardless of the position of these clumps, there would always be several cell pairs that would have to subdivide several times before they become ”resolvable”. In other words, my hypothesis is that the algorithm would not perform well if the dataset has several tight clumps. Why is my reasoning wrong here?

Response: We hope by our responses to comment R1-2 with the example illustrated in Fig. 1 in the previous page, the reviewers are convinced that *clumping by itself does not necessarily cause trouble to our algorithm.*

Although we believe the existence of clumps is not the sufficient condition of a "bad" case, we do agree with the reviewer that the "bad" cases are more common than we previously described. In fact, we never meant to give the impression that the pattern given by Fig. 14 in the previous draft is the only example one can find for a "bad" pattern. We have modified Section 6.1.3 and Fig. 14 (Fig. 15 in the new draft) accordingly.

As to the second paragraph of this comment, we are not absolutely sure what the reviewer meant by "regardless of the position of these clumps, there would always be several cell pairs that would have to subdivide several times before they become resolvable". As we have pointed out before, the cell "resolvability" is not related to data distribution (therefore the existence of clumps). We speculate this was caused by the confusion about how the height of the quad-tree is set. We hope our responses to R1-1 have cleared the doubts.

R1-4. *Let us look at Figure 16. Now, the authors say that Zipf distribution is skewed data. Can the authors explain how/why the "density map level" of Zipf data is identical to the "uniform" distributed data? Moreover, the resolved number of distances also look the same.*

If there is skewness in the data where is it being manifested? All the plots for uniform distribution looks similar to Zipf distribution. How about running experiments on datasets where there are several tight clumps?

Response: Both uniform and Zipf datasets have the same number of density map levels because the latter is only related to N, not to the data distribution. See our responses to comment R1-1 for more details. The resolved number of distances are similar because: 1) in both experiments, the rates of distance consumption are indeed close to 0.5 as m grows, showing the effects of the Zipf distribution in the particular experimental setup are minimal; 2) differences do exist in the absolute values of consumed distances of the uniform and skewed datasets, but they are concealed by the logarithmic scale of the y axle in Fig. 16.

The Zipf distribution we used in Fig. 16-18 was of order 1.0 - we believe such a dataset is by all means "skewed". For the impact of datasets that are extremely skewed (i.e., Zipf with order 2 - 4, mixed Gaussian with small standard deviations), please see our new experimental results and relevant discussions in Section 7.4. Such datasets essentially consist of a very small number of clumps that are extremely "tight".

R1-5. *"We can easily argue that there is no dependency between these two processes therefore the latter will not favor any particular type of cell pairs (e.g., those with higher chance to be resolved, or not to be resolved)."*

I agree with the "no dependency" clause that the authors use here, but argue that while the authors have done a superb job understanding the first aspect of the problem, they do a poor job with the second part (i.e., how point distribution affects running time). The point distribution in a cell decides how much of additional effort has to be expended to make the cell resolvable.

Response: In this statement, we meant to discuss the effects of regular data distribution. For example, if we say the data follows a Zipf or 80/20 distribution, then it generally will not cause any trouble to DT-SDH. In order to create a "bad" case for DT-SDH, we have to put more conditions such as "a Zipf distribution where the distance between two clusters is exactly *ip*". The idea expressed in this statement is elaborated in Section 6.1.3 and in our responses to comments R1-2 and R1-3. In the new draft, this statement was rephrased to reflect our thoughts.

The last sentence of this comment is not correct. We should say "The point distribution in a cell decides how much of additional effort has to be expended to process all the distances related to the cell." Again, we suspect this was caused by the confusion about the tree height H and hope we have resolved that issue.

0.2 Reviewer 3

R3-1. *I am not fully convinced that the analysis can be applied to non-uniform data. E.g., when you increase N to s^dN, the distribution of points within the new four cells (a1-a4 in Fig 12) should resemble the distribution of cells among the sibling of the current cell in the dataset with N points. Therefore, either you are effectively making the assumption of global uniformity or the number of points in a_i will not be the same.*

Response: Please see our responses to R1-1 and R1-2 as well as the newly added analytical and experimental results for the performance of DT-SDH under skewed datasets.

The concept of cell-wise uniform is clearly stated in Section 6.1. It only requires all a_i be the same and all b_i be the same, but $a_i = b_i$ is not required. The latter has to be true for global uniform distribution. As an example of cell-wise uniform, we can imagine a simulation space that is divided into two and only two cells A and B. If we assume A and B are uniform but with different data densities, the data distribution is cell-wise uniform. In studying the time complexity of DT-SDH, we ask the question: when both A and B get a 4-fold increase in their data intensities, how does the running time of the algorithm change? Here, the new cells a1 - a4 only need to follow the data distribution of their parent, and this for sure generates a data that is not globally uniform. The case suggested by the reviewer to follow distribution in the siblings of their parent is not what we meant by "cell-wise uniform". We believe the scenario suggested by reviewer 1 is an example of such dataset with recursive patterns, and we have discussed the impact of that data pattern in our responses to comments R1-1 and R1-2.

R3-2. *I think one of the worst case for your argument (interestingly probably not for your algorithm) is that most data lines on the x-axis while the rest of the data sparsely distributed uniformly in the space. I conjecture that the runtime could be close to $N \log N$?*

Response: We'd appreciate more elaborations on this case. Just by looking at the specified data distribution, we are not as optimistic as the reviewer who sees a $N \log N$ running time of the algorithm.

R3-3. *I think it will be more safe to state sth like: Theorem 3 can be true under XYZ assumption.*

Response: We agree with the reviewer that safe statements should be made. Actually, Theorem 3 itself was presented in an even more conservative way by only saying it works under system-wise uniform distribution. We tend to keep it that way.

R3-4. *Your analysis effectively assumes the cell A is located in the center of the dataset, hence there is no need to consider the effect of boundaries. It is possible that your analysis will be less accurate when number of dim is high as more points will be located around boundaries.*

Response: Yes, in our analysis, we implicitly assumed that cell A is not on the edge of the simulation space. However, we do not see that as a major flaw in our maths as we believe the errors it brings will be minimal. Recall that the non-coverable regions are modeled as rings (in 2D). Theorem 2 tells us that $\alpha(m)$ is proportionally related to the "width" or "thickness" of such rings. Therefore, the situation of having partial rings due to A's locating on the boundary of the simulation space will not change much. We could probably study the magnitude of such errors in an analytical way but that will make the paper too bulky while generating very little extra value.

R3-5. *Sec 8: It is desirable to provide more details on how zipf dataset is generated and how real datasets are duplicated. It is also desirable to use more skewed dataset, e.g., mixed Guassian*

Response: We have added more details about data generation in Section 7.1. We have also performed experiments using high-order Zipf and mixed Gaussian distributions, and the results are reported in Section 7.4.

R3-6. *curves in the figures are hard to distinguish when printed out.*

Response: We have increased the weight of all lines in the figures to make them more readable.

Noname manuscript No.
(will be inserted by the editor)

Performance Analysis of A Dual-Tree Algorithm for Computing Spatial Distance Histograms

Shaoping Chen · Yi-Cheng Tu · Yuni Xia

Received: date / Accepted: date

Abstract Many scientific and engineering fields produce large volume of spatiotemporal data. The storage, retrieval, and analysis of such data impose great challenges to database systems design. Analysis of scientific spatiotemporal data often involves computing functions of all point-to-point interactions. One such analytics, the spatial distance histogram (SDH), is of vital importance to scientific discovery. Recently, algorithms for efficient SDH processing in large-scale scientific databases have been proposed. These algorithms adopt a recursive tree-traversing strategy to process point-to-point distances in the visited tree nodes in batches, thus require less time as compared to the brute-force approach where all pairwise distances have to be computed. Despite the promising experimental results, the complexity of such algorithms has not been thoroughly studied. In this paper, we present an analysis of such algorithms based on a geometric modeling approach. The main technique is to transform the analysis of point counts into a problem of quantifying the area of regions where pairwise distances can be processed in batches by the algorithm. From the analysis, we conclude that the number of pairwise distances that are left to be processed decreases exponentially with more levels of the tree visited. This leads to the proof of a time complexity lower than the quadratic time needed for a brute-force algorithm, and builds the foundation for a constant-time approximate algorithm. Our model is also general in that it works for a wide range of point spatial distributions, histogram types, and space partitioning options in building the tree.

Keywords scientific databases · correlation function · quad tree · spatial distance histogram

Shaoping Chen
Department of Mathematics, Wuhan University of Technology, 122 Luosi Road, Wuhan, Hubei, 430070, P. R. China
Tel. : +86-27-8765-1213 E-mail: chensp@whut.edu.cn
Work was done when Chen was a visiting professor at the University of South Florida.

Yi-Cheng Tu
Department of Computer Science and Engineering , The University of South Florida, 4202 E. Fowler Ave., ENB118, Tampa, FL 33620, U.S.A.
Tel.: +1-813-974-2114, Fax: +1-813-974-5456, E-mail: ytu@cse.usf.edu
Corresponding author.

Yuni Xia
Computer and Information Science Department, Indiana University - Purdue University Indianapolis, 723 W. Michigan St, SL280, Indianapolis, IN 46202, U.S.A.
Tel. : +1-317-274-9738, Fax: +1-317-274-9742, E-mail: yxia@cs.iupui.edu

1 Introduction

The development of advanced experimental devices and computer simulations have given rise to explosive rendering of data in almost all scientific fields. As a result, scientific data management has gained much momentum in the database research community. Recent years have witnessed increasing interest in developing database systems for the management of scientific data [11,33,19,23,15,13,39,40]. While taking advantage of the optimized I/O and querying power of relational DBMSs, such systems still fall short of algorithms and strategies to satisfy the special needs of scientific applications, which are very different from traditional database applications in their data types and query patterns. In this paper, we are interested in query processing against *scientific spatiotemporal data*. Such data are very popular in various scientific [14,2,31] and engineering [22] fields where natural systems (e.g., cells, galaxies) are often studied by computer simulations performed on the

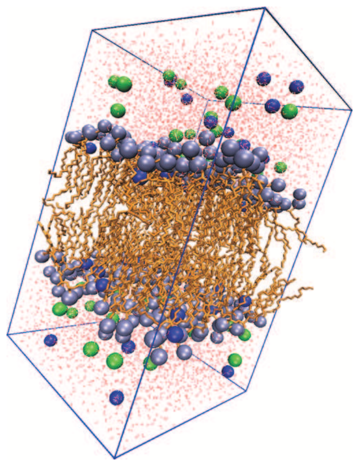

Fig. 1 A simulated hydrated dipalmitoylphosphatidylcholine bilayer system. We can see two layers of hydrophilic head groups (with higher atom density) connected to hydrophobic tails (lower atom density) are surrounded by water molecules (red dots) that are almost uniformly distributed in space.

level of basic system components (e.g., atoms, stars). By nature, such applications generate very large datasets. For example, molecular simulations often deal with systems with up to millions of atoms (Fig. 1). As a case of extreme, the Virgo consortium recently accomplished a simulation that consists of 10 billion stars [30].

Apart from the challenges of data storage/retrieval imposed by the gigantic volume of scientific data, we also face the issue of designing efficient algorithms for data querying and analysis. Scientific data analysis often require computation of mathematical (statistical) functions [17,11] whose complexity goes beyond simple aggregates, which are the only analytics supported by modern DBMSs. Many complex analytics in scientific applications are found to be hierarchical in that they are often defined on top of a small number of low-level analytics as building blocks. Therefore, it is desirable to have built-in support for efficient processing of such low-level analytics in the DBMS. One salient example of such analytics is the *n-body correlation functions* (n-BCF). Generally, an n-BCF is a statistical measure of all the n-point subsets of the whole dataset. In a dataset with N data points, an n-BCF requires $O(N^n)$ time to compute in a brute-force way.

One type of 2-BCF query called the *Spatial Distance Histogram* (SDH) is of vital importance in computational sciences and thus the focus of this paper. The SDH problem can be formally stated as follows.

> *Given the coordinates of N particles in a (2D or 3D) metric space, draw a histogram that represents the distribution of the pairwise distances between the N points.*

The histogram has a single parameter l, which is the total number of buckets. Since the dataset is always generated from a system with fixed dimensions, the maximum distance between any two points L_{max} is also fixed. We often deal with *standard SDHs* whose buckets are of the same width. The width of the buckets (i.e., histogram resolution) $p = L_{max}/l$ is often used as the parameter of the query instead. In other words, SDH asks for the counts of pairwise distances that fall into ranges $[0, p), [p, 2p), \cdots, [(l-1)p, lp]$, respectively. Basically, SDH is a discrete representation of a continuous 2-BCF called *Radial Distribution Functions* (RDF) [4,31]. The latter is required for the computation of many critical high-level analytics such as pressure, energy, [14] and structure factor [12]. Without RDF, meaningful analysis of the physical/chemical features of the studied natural system is not possible.

While a naive way to compute SDH takes $O(N^2)$ time, more efficient algorithms have been proposed in our previous work [38] and in the data mining community [16,25]. As summarized in Section 2.3, the main idea of this type of algorithms is to derive the histogram by studying the distances between two clusters of particles instead of those between two individual points. The clusters are represented by nodes in a space-partitioning tree structure. Although different implementations exist in [16,25] and [38], such an approach can be abstracted into a recursive tree-based algorithm described in Section 3. Since the recursion always happens between two disjoint subtrees, these algorithms are called *dual-tree algorithms* [16]. While experimental results support the efficiency of such algorithms, their complexity has not been thoroughly studied. In this paper, we present an analytical model to accomplish quantitative analysis of the performance of this algorithm. The main technique is to transform the analysis of particle counts into a problem of quantifying the area of interesting geometric regions. Our analysis not only leads to a rigorous proof of the algorithm's time complexity, but also builds the foundation for approximate algorithms [38,16]. With time complexity that depends only on a controlled error bound, such algorithms are the only practical solutions to SDH computation in large datasets. Although we focus on a specific 2-body correlation function, the dual-tree algorithm can be easily extended to handle higher order correlation functions [25]. Furthermore, the significance of this work is not limited to scientific databases: the dual-tree algorithm is also used to process a series of queries useful in data mining, such as batch k-nearest neighbor, outliner detection, kernel density estimation, and k-means [16].

Paper organization This paper is organized as follows: in Section 2, we summarize the contributions of this paper via comparison to related work; in Section 3, we sketch the dual-tree algorithm; we present our basic analytical model in Section 4 and two important extensions of the model in Section 5; we show an analysis of the time complexity of the dual-tree algorithm in Section 6; we report experimental results in Section 7, and conclude our paper in Section 8.

2 Related Work and Our Contributions

2.1 Scientific Data Management

The scientific community has been in a transition from developing *ad hoc* data processing systems based on flat files to utilizing modern database technology for data management tasks. There is a large number of scientific databases built on top of existing relational DBMSs. Well known examples include: the GenBank[1] database provides public access to about 80 million gene sequences; the Sloan Digital Sky Survey [33] enables public access to more than 100 attributes of 200 million objects in the sky; the QBISM project [3] delivers a prototype of querying and visualizing 3D medical images; and the Stanford Microarray Database[2] is a portal for storing and querying gene expression data.

However, scientific data are different from traditional data in that: (1) the volume of scientific data can be orders of magnitude larger; (2) data are often multidimensional and continuous; and (3) queries against scientific data are more complex. While the basic database system architecture can still be adapted, the above differences bring significant challenges to DBMS design. To meet such challenges, the database community has taken two different paths. The first one is to address domain-specific data management issues by modifying particular modules of existing relational DBMSs. There is a series of work dedicated to various aspects such as I/O scheduling [24], query processing [9,28] and data provenance management [10]. Another thrust is to build a general-purpose platform from scratch to support a wide range of scientific applications [32,21,6]. The work presented in this paper falls into the first category by emphasizing efficient processing of a special yet highly useful analytical query.

[1] http://www.ncbi.nlm.nih.gov/Genbank
[2] http://smd.stanford.edu/

2.2 Computation of Force/Potential Fields

The SDH/RDF problem is often confused with another group of problems — the computation of force/potential fields in scientific simulations. Specifically, the physical properties of a system component (represented as a point in space) is determined by the force applied to it by all other points in the system. Therefore, to compute the force applied to all points, $O\big(N^2\big)$ time is required. Since the force/potential can be expressed as an empirical integration formula, much efforts have been devoted to efficient force computation from a numerical analysis viewpoint. Most of the research in this field are derived from two lines of work: the Barnes-Hut algorithm [5] that requires $O\big(N \log N\big)$ time, and the fast multi-pole algorithm [18] with linear time complexity. These methods utilize unique features of the force (e.g., symmetry and fast degradation with distance) to bound the computational errors. However, they provide little insights to the SDH problem as the latter lacks such features.

Another method based on well-separated pair decomposition (WSPD) was proposed by Callahan and Kosaraju [7]. The WSPD is a series of pairs of subsets of the data points. Each pair of subsets P_i and P_j are well-separated: the distance between the smallest balls (with radius r) covering the particles in P_i and P_j is at least sr where s is a system-level parameter. Following the algorithm in [7] that also utilizes a space-partitioning data structure called *fair-split tree*, the WSPD can be built in $O(N \log N)$ time and there are only $O(N)$ such pairs of subsets that cover all pairs of particles. As a result, the force fields can be computed in $O(N)$ time, given the WSPD. It may look intuitive that a WSPD can also be used to compute SDH: for each subset pair, their point-to-point distances fall into the range $[rs, rs + 4r]$; by carefully choosing s and r, we can fit this range into relevant buckets of the histogram. However, the pitfall here is: s is a configurable parameter of the WSPD construction algorithm while r is not — it can be any value in each pair of subsets. If we enforce a specific value for r, the $O\big(N\big)$ performance guarantee is lost. Therefore, it does not provide a shortcut to efficient SDH processing to use the WSPD. In summary, the difficulty of the SDH problem is to put distances into buckets with clearly defined boundaries (Section 6.1) while the WSPD can only be manipulated to work with fuzzy ranges.

2.3 Algorithms for Efficient SDH Computation

Despite the importance of SDH, efficient SDH processing has not been intensively studied. Popular simulation data analysis softwares such as GROMACS [20] still follow the brute-force way to compute SDH. In [34] and [35], the SDH is processed by dividing the simulation space into bins and treating each bin as a single entity and run quadratic algorithms on these bins. Such an approximate solution, while reducing the computation time, can obvious yield uncontrollable errors. One approach to get the exact SDH is to issue a series of range queries (i.e., one for each bucket) for each data point, taking advantage of the *kd*-trees for range queries. This method, so called the **single-tree algorithm**, was extended to the **dual-tree algorithm** where the *kd*-trees are still used [16]. In our previous work [38], we utilized the Quad/Oct-tree to divide the simulation space into equally-sized cells and used it explicitly for SDH processing. The main idea behind the dual-tree algorithm is to process clusters of particles to take advantage of the non-zero width of the SDH bucket. The name "dual-tree" comes from the fact that it always works on a pair of such clusters (i.e., subtrees) while the single-tree algorithm on one data point and one subtree. Note that the *kd*-tree is equivalent to a Quad-tree if we assume the particles are uniformly distributed in space. However, it turns out the use of Quad-tree is critical to achieve rigorous analysis. In addition to convincing experimental results, both work reported results of some asymptotical analysis. However, the results in [16] come with no technical details at all while our earlier paper [38] only sketched the main analytical results.

2.4 Contributions of This Work

This paper significantly extends [38] by introducing the models behind the analytical results. In summary, this paper makes the following contributions.

1. We present details of an analytical model based on a geometric modeling approach. Such content are not found in any previous work;
2. The results in [16] and [38] are strictly based on the assumption that particles follow a uniform spatial distribution in space. This assumption is obviously unreasonable in real simulation environments. We relax this assumption in our analysis;
3. We present an extended model for performance analysis in 3D space; and
4. We extend the analysis to arbitrary space partitioning parameters (i.e., node degree) in building the spatial tree.
5. We also show the dual-tree algorithm has the same time complexity in processing SDHs with variable bucket width.

3 The Dual-Tree Algorithm

In this section, we present the main idea of the dual-tree SDH algorithm (DT-SDH). DT-SDH is an abstraction of both methods presented in [16] and [38]. With the assumption of uniform particle distribution, the *kd*-tree in [16] is equivalent to a region Quad-tree, which is explicitly used in [38] and also the abstracted DT-SDH algorithm.

```
Procedure ResolveTwoTrees ($\mathcal{A}$, $\mathcal{B}$)
1  if $\mathcal{A}$ and $\mathcal{B}$ are resolvable
2      add $n_a n_b$ to the corresponding bucket
3  elseif $\mathcal{A}$ and $\mathcal{B}$ are not leaf nodes
4          for each child a of $\mathcal{A}$
5              for each child b of $\mathcal{B}$
6                  ResolveTwoTrees (a, b)
7  else
8      compute all point-to-point distances between $\mathcal{A}$ and $\mathcal{B}$
       and add each pair to the corresponding bucket
```

Fig. 2 Procedure ResolveTwoTrees - core of the DT-SDH algorithm.

The algorithm first divides the simulated space into a grid, each cell of which records the number of data points in it. We call such a grid a *density map* and density maps with different cell sizes have to be maintained. We therefore organize all point coordinates into a point region Quad-tree [27] with each node representing a cell (square for 2D data and cube for 3D) in space. Point counts of each cell are cached in the corresponding tree node. Those with zero point count are removed from the tree. The height of the tree (denoted as H) is determined in a way such that the *average* number of points in all possible leaf nodes is no smaller than a predefined threshold β. To be specific, we have

$$H = \left\lceil \log_{2^d} \frac{N}{\beta} \right\rceil \tag{1}$$

where d is the number of dimensions and 2^d is essentially the maximal degree of tree nodes.

The focal point of this algorithm is a procedure named ResolveTwoTrees (Fig. 2). To resolve two cells $\mathcal{A}$ and $\mathcal{B}$ (with total particle counts n_a and n_b, respectively), we first read the coordinates of the two cells and compute the range of distances between any pair of points, one from $\mathcal{A}$ and one from $\mathcal{B}$. Note that, given the coordinates of the two cells, this distance range can be computed in constant time (Fig. 3). If this range is contained in the range of a histogram bucket i, we say $\mathcal{A}$ and $\mathcal{B}$ are *resolvable* and they *resolve into* bucket i. In this case, we simply increment the count of bucket i by $n_a n_b$ (line 2). If the two cells are not resolvable, we

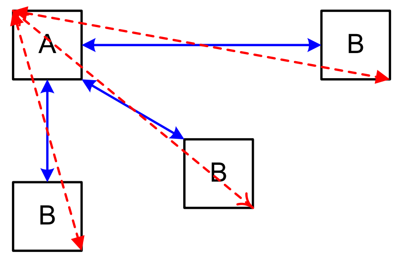

Fig. 3 Three scenarios in computing the minimum and maximum distance between two cells A and B, with solid (dotted) line representing minimum (maximum) distance in each case.

Table 1 Notations and definitions.

Symbol	Definition
N	total number of particles in data
l	total number of histogram buckets
p	width of histogram buckets
m	an index of the density map (level on the Quad-tree)
i	an index on histogram buckets
δ	side length of the cells on DM_0
$\alpha(m)$	non-covering factor on level DM_m
S	the area of some region
s	tiling factor
d	number of dimensions in data (up to 3)

recursively resolve all pairs of their child nodes (line 6). It is easy to see that, no matter how small the cells are in a density map, non-resolvable cell pairs always exist. Therefore, when we reach the lowest level of the tree, we have to calculate all distances of the particles in the unresolved cells (line 8).

In practice, β is set to be around 2^d. The intuition behind that is, when a pair of non-resolvable cells contains less than 16 (64 for 3D) distances (i.e., roughly 4 points in each cell), it does not help to further divide them. The process of tree construction can be accomplished in $O(N \log N)$ time.

The algorithm starts from a certain level of the tree where the diagonal of the cells is no greater than the bucket width p. We denote this level as density map DM_0. In other words, we require

$$\delta \le \frac{p}{\sqrt{d}} \tag{2}$$

where δ is the side length of the cells in DM_0 and d is the number of dimensions in the data. Note that no cells can be resolved if the above inequality does not hold true. The dual-tree algorithm runs as: first, all intra-cell particle-to-particle distances on DM_0 can be put into the first bucket $[0, p)$, as p is larger than the cell diagonal; second, ResolveTwoTrees is executed for all pairs of non-empty cells on DM_0.

3.1 Basic Ideas in Analyzing DT-SDH

The running time of DT-SDH is consumed by the following two types of operations:

(i) checking if two cells are resolvable (i.e., line 1 in ResolveTwoTrees); and
(ii) distance calculation for data points in cell pairs that are non-resolvable even on the finest density map (i.e., line 8 in ResolveTwoTrees).

As compared to the brute-force algorithm, we perform type (i) operations in hope of handling multiple distances in one shot such that the number of type (ii) operations is minimized. Given a histogram bucket width p, we start from a density map DM_0 with c cells. Thus, there are $O(c^2)$ type (i) operations to be performed on level DM_0. On the next map DM_1, there are $4 \times 4 = 16$ times of cell pairs to resolve. However, some of the cells in DM_1 do not need to be considered as their parents are resolved on DM_0. From this, we can easily see that the running time has something to do with p since it determines the number of cells in DM_0. However, in analyzing the time complexity of DT-SDH, we are interested in how the running time increases as the total number of points N increases, as p is a fixed query parameter. Qualitatively, as N increases, the height of the quad-tree also increases (due to a fixed β), giving rise to a higher percentage of resolvable cell pairs on the leaf level. On the other hand, the total number of cell pairs also increases (quadratically). An essential question our analysis needs to answer is: given a cell **A** on DM_0, how many pairs of points are contained by those resolvable cells related to **A** as we visit more and more levels of density maps? Although this apparently has something to do with the spatial distribution of the points, our main idea is to first analyze *how much area are covered by the resolvable cells* to simplify the process, and then discuss the effects of particle spatial distribution on this basic analysis. In the following section, we use a geometric modeling approach to quantify the area of resolvable cells of interest. Some of the symbols used throughout this paper are listed in Table 1.

4 Main Analytical Results

4.1 Overview of Our Approach

Given any cell **A** on density map DM_0, our analysis first quantifies the area of a theoretical region containing all particles that can possibly resolve into the ith bucket with any particle in **A**. We call this region the *bucket i region* of cell **A** and denote it as $\mathbf{A_i}$. In a 2D example

Table 2 Values of $\alpha(m+1)/\alpha(m)$ in 2D space under different values of m and l. Computed with Mathematica 6.0 based on the formulae generated in Section 4.4. Precision up to the 6th digit after decimal point.

Map	**Total Number of Histogram Buckets (l)**						
levels	2	4	8	16	32	64	256
m=1	0.508709	0.501837	0.50037	0.50007	0.500012	0.500002	0.5
m=2	0.503786	0.500685	0.500103	0.500009	0.499998	0.499999	0.5
m=3	0. 501749	0.500282	0.500031	0.499998	0.499997	0.499999	0.5
m=4	0. 500838	0.500126	0.50001	0.499997	0.499998	0.499999	0.5
m=5	0. 50041	0.500059	0.500004	0.499998	0.499999	0.5	0.5
m=6	0.500203	0.500029	0.500002	0.499999	0.499999	0.5	0.5
m=7	0.500101	0.500014	0.500001	0.499999	0.5	0.5	0.5
m=8	0.50005	0.500007	0.5	0.5	0.5	0.5	0.5
m=9	0.500012	0.500003	0.5	0.5	0.5	0.5	0.5
m=10	0.500025	0.500002	0.5	0.5	0.5	0.5	0.5

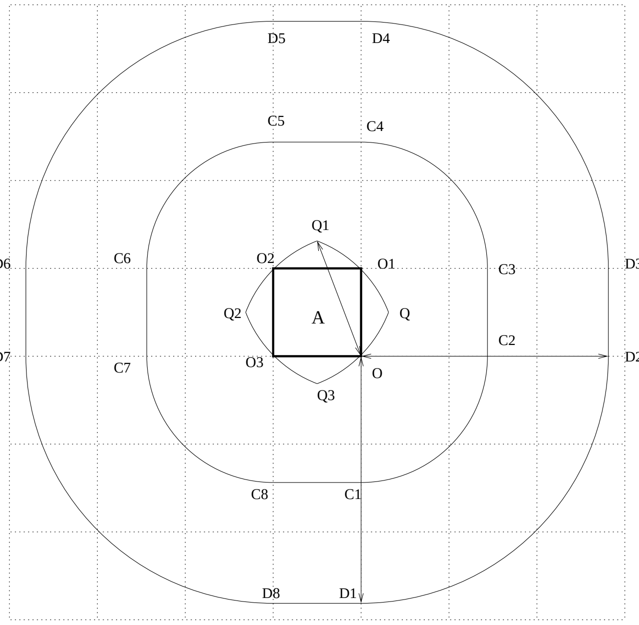

Fig. 4 Boundaries of bucket 1 and bucket 2 regions of cell **A**, with the bucket width p being exactly $\sqrt{2}\delta$. Here we show arcs $\widehat{Q_1Q_2}$, $\widehat{C_1C_2}$, and $\widehat{D_1D_2}$, all of which are centered at point O.

illustrated in Fig. 4, a cell **A** is drawn with four corner points O, O_1, O_2, and O_3, and $\mathbf{A_1}$ is bounded by curves and line segments connected by points C_1 through C_8. In our analysis, we consider the boundary situation of formula (2): the side length of cell **A** is set to be exactly $\delta = \frac{p}{\sqrt{2}}$. As we can easily see later, the case of $\delta < \frac{p}{\sqrt{2}}$ will not change the analytical results. Technical details on the quantification of the area of $\mathbf{A_i}$ is presented in Section 4.2.

The cells that are resolvable into bucket i with any subcells in **A** also form a region. We call such region the *coverable region* and denote it as $\mathbf{A_i'}$. Due to the shape of subcells, the boundary of such regions shows a zigzag pattern, as represented by solid blue lines in Fig. 6. When DT-SDH visits more levels of the tree, the resolution of the density map increases, and the boundary of region $\mathbf{A_i'}$ approaches that of $\mathbf{A_i}$. The quantification of the coverable regions' area is discussed in Section 4.3.

With the above results, we then study the area of coverable regions over all buckets and how the density map resolution affects it. Specifically, we define the ratio of $\sum_i \mathbf{A_i'}$ to $\sum_i \mathbf{A_i}$ as the *covering factor*. This is a critical quantity in our analysis as it tells how much area are "covered" by resolved cells. Obviously, the covering factor increases when we visit more levels of density map. Of special interest to our analysis is the *non-covering factor*, which represents the percentage of area that is not resolvable. The details about covering factor can be found in Section 4.4. A very important feature of the non-covering factor can be summarized in the following theorem.

Theorem 1 *Let DM_0 be the first density map the* DT-SDH *algorithm starts running, and $\alpha(m)$ be the percentage of pairs of cells that are not resolvable on the density map that lies m levels below DM_0 (i.e., map DM_m). We have*

$$\lim_{p \to 0} \frac{\alpha(m+1)}{\alpha(m)} = \frac{1}{2}.$$

Proof The proof is developed in the remainder of this section starting from subsection 4.2.

While shown in the form of a limit under large l (i.e., small p), Theorem 1 also works well under small l values. This can be effectively verified by numerical results obtained from the closed-form formulae we derive (Eq. (9) and Eq. (10)) to accomplish the proof. In Table 2, we can easily see that the ratio of $\alpha(m+1)$ to $\alpha(m)$ quickly converges even when l is very small.

Theorem 1 is important in that it shows the number of non-resolvable cell pairs decreases exponentially (by half) when more levels of the tree are visited. In ResolveTwoTrees, if a cell pair is not resolved, we have to make 16 recursive calls to the same routine for the 4 children of each cell. Theorem 1 says that we can

$$g(i) = \begin{cases} (2\pi + 4\sqrt{2} + 1)\delta^2 & i = 1 \\ \left[2\pi i^2 + 4\sqrt{2}i - (i-1)^2\left(8\arctan\sqrt{8(i-1)^2-1} - 2\pi\right) + \sqrt{8(i-1)^2-1}\right]\delta^2 & i > 1 \end{cases} \tag{3}$$

expect $16 \times 0.5 = 8$ pairs of the child nodes to be resolvable. For these resolved cell pairs, there is no need to further explore the pair of subtrees rooted by them. This greatly eases our analysis of the time complexity of DT-SDH (Section 6).[3] Now let us consider a formal proof of Theorem 1.

4.2 Maximal bucket region

As mentioned earlier, the bucket 1 region for cell **A** in Fig. 4 is connected by C_1 through C_8. Specifically, C_1C_2, C_3C_4, C_5C_6, and C_7C_8 are all 90-degree arcs centered at the four corners of cell **A** and their radii are of the same value p; C_2C_3, C_4C_5, C_6C_7, and C_8C_1 are line segments. It is easy to see that the area of this region is $\pi p^2 + 4p\delta + \delta^2$. Let us continue to consider distances that fall into the second bucket (i.e., [p, 2p)). Again, the bucket 2 region of **A** is of similar shape to the bucket 1 region except the radii of the arcs are $2p$, as drawn in Fig. 4 with a curve connected by points $D_1, D_2, \ldots, D_8$. However, points that are too close to **A** can only resolve into bucket 1 since their distances to any point in **A** will always be smaller than p. These points are contained in a region as follows: on each corner point of **A**, we draw an arc with radius p on the opposite corner (i.e., arcs QQ_1, Q_1Q_2, Q_2Q_3, and Q_3Q). Therefore, the bucket 2 region should not include this inner region (denoted as region **B** hereafter, see Fig. 5 for a magnified illustration).

The area of the bucket 2 region is $\pi(2p)^2 + 8p\delta$ less the area of region **B**, which consists of eight identical smaller regions such as $\widehat{Q_1O_2}D$ (Fig. 5) and cell **A** itself. To get the area of $\widehat{Q_1O_2}D$, we first compute the magnitude of the angle $\angle Q_1OO_2$ as follows.

$$\angle Q_1OO_2 = \angle Q_1OE - \angle COE = \arctan\frac{Q_1E}{EO} - \frac{\pi}{4}$$
$$= \arctan\frac{\sqrt{p^2 - \left(\frac{\delta}{2}\right)^2}}{\frac{\delta}{2}} - \frac{\pi}{4}$$

Thus, the area of sector $\widehat{Q_1O_2}O$ is $\frac{1}{2}p^2\angle Q_1OO_2$. The area of region $\widehat{Q_1O_2}D$ can be obtained by the area of this sector less the area of triangles O_2DC and Q_1CO as follows:

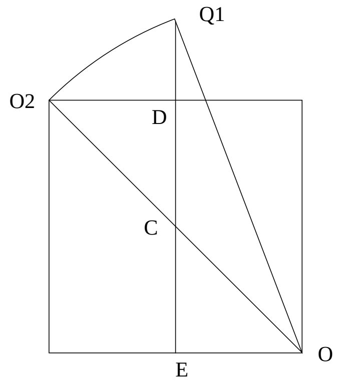

Fig. 5 A magnification of region **B** (i.e., $QQ_1Q_2Q_3$ formed by four arcs in Fig. 4). Here we only show arc Q_1O_2, which is a half of arc Q_1Q_2.

$$S_{\widehat{Q_1O_2}D} = S_{\widehat{Q_1O_2}O} - S_{\triangle O_2DC} - S_{\triangle Q_1CO}$$
$$= \frac{1}{2}p^2\left[\arctan\frac{2\sqrt{p^2 - \left(\frac{\delta}{2}\right)^2}}{\delta} - \frac{\pi}{4}\right]$$
$$-\frac{\delta}{4}\sqrt{p^2 - \left(\frac{\delta}{2}\right)^2}$$

and we have $\pi(2p)^2 + 8p\delta - 8S_{\widehat{Q_1O_2}D} - S_{\mathbf{A}}$ as the area of the bucket 2 region.

The approach to obtain the area of bucket i $(i > 2)$ regions is the same as that for bucket 2. For the area of the region formed by the outer boundary, we only need to consider that the arcs in Fig. 5 are of radii ip. Along with the fact $p = \sqrt{2}\delta$, our efforts lead to a general formula to quantify the area of the bucket i region in Eq. (3) shown on top of this page.

4.3 Coverable regions

The are two different scenarios to consider in deriving the area of coverable regions.

4.3.1 Case 1: the first bucket

Let us start our discussions on the situation of bucket 1. In Fig. 6, we show the coverable regions of three different density map levels: $m = 1$, $m = 2$, and $m = 3$, as represented by blue-colored lines and denoted as $\mathbf{A}'$ in

[3] The techniques to derive Theorem 1 are important. However, readers can get a big picture of this work by browsing Theorem 2 (a more general form of Theorem 1) in Section 5.2 and then moving to Section 6.

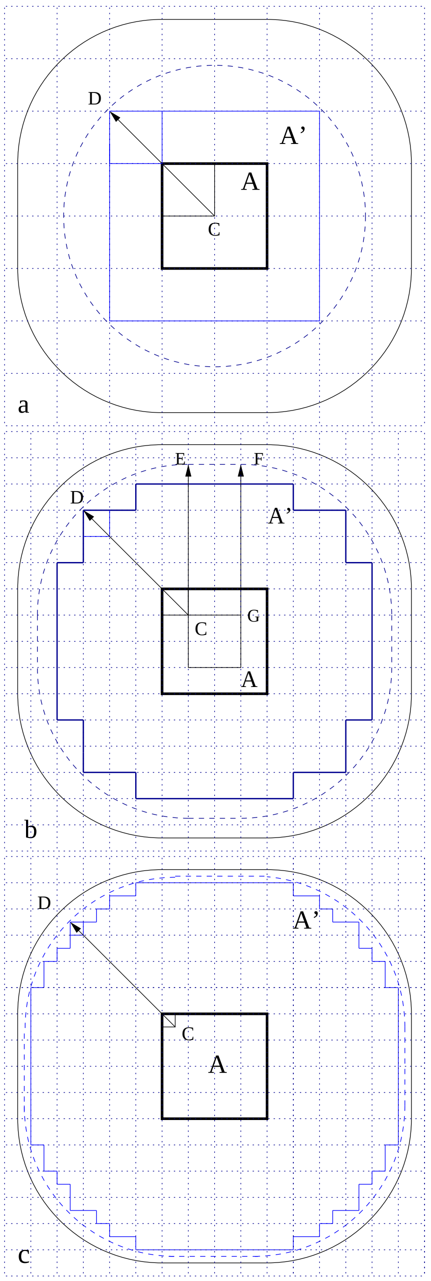

Fig. 6 Actual (solid blue line) and approximated (dotted blue line) coverable regions for bucket 1 under: a. $m = 1$; b. $m = 2$; and c. $m = 3$. Outer solid black lines represent the theoretical bucket 1 region. All arrowed line segments are drawn from the centers to the corresponding arcs with radius p.

all subgraphs. Recall that, for two cells to be resolvable into bucket i, the minimum and maximum distance between them should both fall into range $[(i-1)p, ip)$. For $m = 1$, the resolvable cells are only those surrounding **A**. All other cells, even those entirely contained by the bucket 1 region, do not resolve with any level 1 subcell of **A**. As we increase m, the region $\mathbf{A}'$ grows in area, with its boundary approaching that of the bucket 1 region. To represent the area of $\mathbf{A}'$, the technique we adopt is to *develop a continuous line to approximate its boundary*. This technique will be used throughout our analysis. One critical observation here is: the furtherest cells in $\mathbf{A}'$ are those that can resolve with cells on the outer rim of **A**. For example, the cell cornered at point D resolves with the cell cornered at point C in **A**. If we draw a 90-degree arc centered at C, the arc goes through D and all cells on the northwestern corner of $\mathbf{A}'$ are bounded by this arc. To approximate the boundary of $\mathbf{A}'$, we can draw such an arc at all four corners of the graph and connect them with line segments (e.g., EF connecting the northwestern and northeastern arcs centered at point G in Fig. 6b), as shown by the blue dotted line. Obviously, this line approaches the theoretical boundary as m increases because the center of the arcs (e.g., point C) move further to the corner points of **A** as the cells become smaller. Note that this line gives rise to an optimistic approximation of $\mathbf{A}'$. In Section 6, we will show that this overestimation will not harm our analysis on the time complexity of DT-SDH. The area of the coverable region for bucket 1 at level m can thus be expressed as

$$S_{\mathbf{A}'} = \pi p^2 + 4p\left(\delta - \frac{2\delta}{2^m}\right) + \left(\delta - \frac{2\delta}{2^m}\right)^2 \qquad (4)$$

where the first item πp^2 is the area of the four 90-degree sectors centered at point C, the second item is the area of the four rectangles (e.g., EFGC in Fig. 6b) connecting the four sectors, and the last item is the area of the smaller square (e.g., the one with side CG in Fig. 6b) within cell **A**.

4.3.2 Case 2: the second bucket and beyond

The cases of buckets beyond the first one are more complicated. First of all, the outer boundary of the bucket i ($i \geq 2$) regions can be approximated using the same techniques we introduced for bucket 1 (Section 4.3.1). To be specific, we can use the following generalized form of Eq. (4) to quantify the area of the region formed by the outer boundaries only.

$$S_{out}(i) = \pi(ip)^2 + 4ip\left(\delta - \frac{2\delta}{2^m}\right) + \left(\delta - \frac{2\delta}{2^m}\right)^2 \qquad (5)$$

However, we also need to disregard the cells that lie in the inner boundary (e.g., those within or near region **B**). This has to be considered in two distinct cases: $m = 1$ and $m > 1$.

Let us first study the case of $m = 1$. Fig. 7 shows examples with $m = 1$ with respect to the second and the third bucket. It is easy to see that any cell that contains a segment of the theoretical region **B** boundary will not

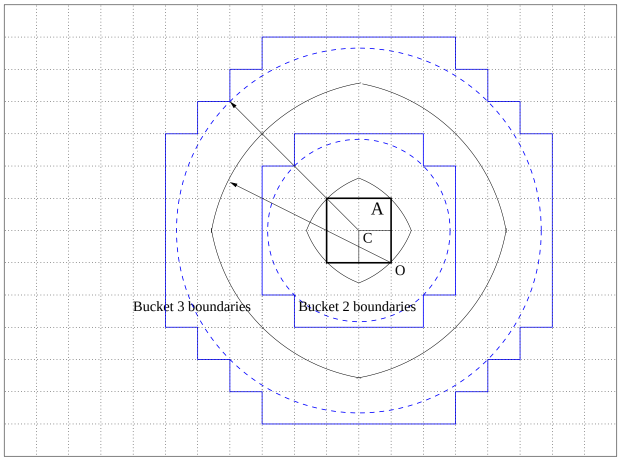

Fig. 7 Inner boundaries of the coverable regions of buckets 2 and 3 under $m = 1$. All arrowed line segments are of length $2p$.

resolve into bucket i because they can only resolve into bucket $i - 1$. Furthermore, there are more cells that resolve into neither bucket $i-1$ nor bucket i. Here our task is to find a boundary to separate those $m = 1$ cells that can resolve into bucket i with any subcell in **A** and those that cannot. Such boundaries for buckets 2 and 3 are shown in Fig. 7 as solid blue lines. The boundary can be generated as follows: on each quadrant (e.g., northwest) of cell **A**, we draw an arc (dotted blue line) centered at the corner point C of the furthest (e.g., southeast) subcell of **A** with radius $(i - 1)p$. Any cell that contains a segment of this arc cannot resolve into bucket i (because they are too close to **A**) but the cells beyond this line can. Therefore, we can also use these arcs to approximate the zigzagged real boundaries. Let us denote the region bounded by this approximate curve as region $\mathbf{B'}$. For $m = 1$, the arcs on all four quadrants share the same center C therefore they form a circle as region $\mathbf{B'}$. The radii of the circles are exactly $(i - 1)p$ for bucket i. Note that this, again, could give rise to an optimistic approximation of the area of coverable regions. Therefore, the area of the coverable region for $m = 1$ and $i \geq 2$ is:

$$S_{\mathbf{A'}} = \pi(ip)^2 - \pi[(i-1)p]^2 \tag{6}$$

where the first item is the area of the region formed by the approximated outer boundary, which is given as a special case of Eq. (5) for $m = 1$ and happens to be a circle; and the second item is that of the region formed by the approximated inner boundary (i.e., region $\mathbf{B'}$).

For the case of $m > 1$, we can use the same technique described for the case of $m = 1$ to generate the curves to form region $\mathbf{B'}$. However, these curves are no longer a series of circles. In Fig. 8, we can find such curves for buckets 2 and 3 under m values of 2 and 3.

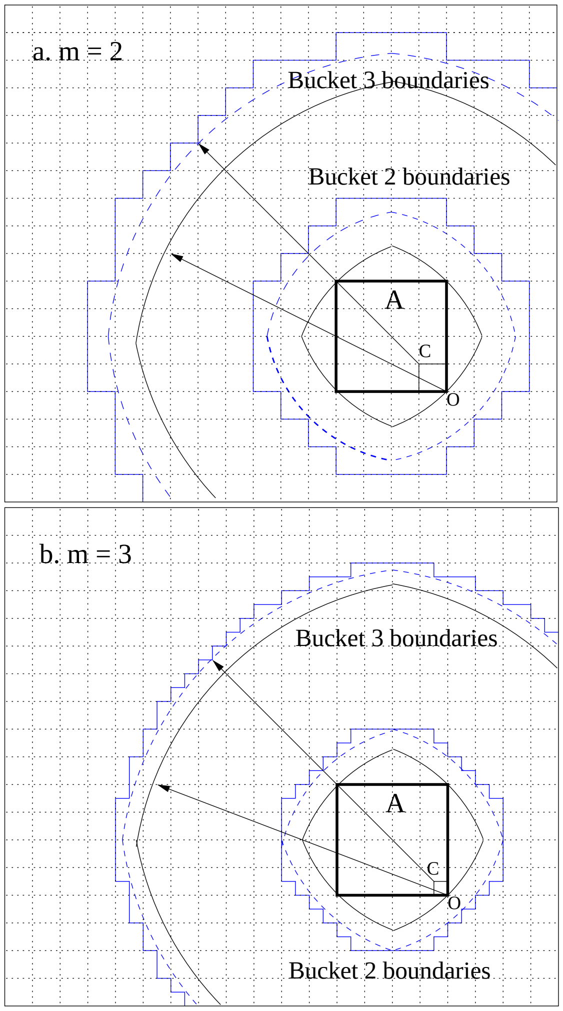

Fig. 8 Inner boundaries of the coverable regions of buckets 2 and 3 under $m = 2$ and $m = 3$. All arrowed line segments are of length $2p$.

As the four arcs on different quadrants no longer share the same center, the region $\mathbf{B'}$ boundaries (dotted blue lines) are of similar shapes to the theoretical region **B** boundaries (solid black lines). From the graphs, it is easy to see that the approximated curve fits the actual boundary better as m increases. Here we skip the formal proof as it is straightforward. Furthermore, it also converges to the region **B** boundary when m gets bigger. This is because the centers of the two arcs (with the same radii), points C and O, become closer and closer when the cell size decreases (as m increases).

The area of region $\mathbf{B'}$ (Fig. 9) can be computed in the same way as that of region **B**. Following that, the area of coverable region for $m > 1$ can be derived. The details of such results can be found in Appendix A. We define θ as a function of m for the convenience in further

$$f(i,m)=\begin{cases}\left[2\pi+4\sqrt{2}+1-(8\sqrt{2}+4)\frac{1}{2^m}+\frac{4}{2^{2m}}\right]\delta^2 & i=1, m\geq 1\\ \left[2\pi(2i-1)\right]\delta^2 & i>1, m=1\\ \left\{2\pi i^2+4\sqrt{2}i-(8\sqrt{2}i+4)\frac{1}{2^m}+\frac{4}{2^{2m}}-8\left[(i-1)^2\left(\arctan\frac{\gamma_m}{\theta_m}-\frac{\pi}{4}\right)-\frac{1}{2}\theta_m\left(\gamma_m-\theta_m\right)\right]+1\right\}\delta^2 & i>1, m>1\end{cases} \quad (7)$$

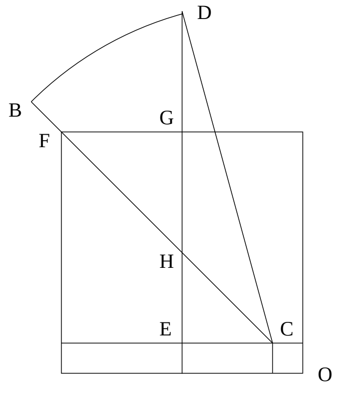

Fig. 9 An illustration on how to compute the area of region formed by four arcs in Fig. 8. Here we only show half of one of the arcs.

discussions:

$$\theta_m=\frac{1}{2}-\frac{1}{2^m}.$$

Let us denote the area of the coverable region $\mathbf{A}'$ for bucket i under different m values as $f(i,m)$. By combining and simplifying Equations (4), (6), and the results in Appendix A with $p=\sqrt{2}\delta$, we get Eq. (7) , in which $\gamma_m=\sqrt{2(i-1)^2-\theta_m^2}$.

4.4 Covering factor and derivation of Theorem 1

In this section, we give a quantitative analysis on the relationship between $f(i,m)$ and the area of the theoretical region $g(i)$ for all buckets. For that purpose, given any density map level m, we define the *covering factor* $c(m)$ as the ratio of the total area of the coverable regions to that of the theoretical bucket i regions over all i. Relate this to Theorem 1, the more interesting quantity is the *non-covering factor*:

$$\alpha(m)=1-c(m)=\frac{\sum_{i=1}^{l}[g(i)-f(i,m)]}{\sum_{i=1}^{l}g(i)} \quad (8)$$

With Eq. (8) and the results we have in Sections 4.2 and 4.3, we are now ready to prove Theorem 1. Recall that we defined $\theta_m=\frac{1}{2}-\frac{1}{2^m}$ and $\theta_{m+1}=\frac{1}{2}-\frac{1}{2^{m+1}}$. Plugging Eq. (3) and Eq. (7) into Eq. (8), we get $\frac{\alpha(m+1)}{\alpha(m)}=\frac{A(m)}{B(m)}$ where

$$\begin{aligned}A(m)=&\frac{2}{2^m}-\frac{1}{4^m}+\frac{2^{\frac{3}{2}}}{2^m}(l+l^2)+\sum_{i=2}^{l}\sqrt{8(i-1)^2-1}\\&-4\sum_{i=2}^{l}\theta_{m+1}\sqrt{2(i-1)^2-\theta_{m+1}^2}\\&+8\sum_{i=2}^{l}(i-1)^2\arctan\frac{\sqrt{8(i-1)^2-\theta_{m+1}^2}}{\theta_{m+1}}\\&-8\sum_{i=2}^{l}(i-1)^2\arctan\sqrt{8(i-1)^2-1}\end{aligned} \quad (9)$$

and

$$\begin{aligned}B(m)=&\frac{4}{2^m}-\frac{4}{4^m}+\frac{2^{\frac{5}{2}}}{2^m}(l+l^2)+\sum_{i=2}^{l}\sqrt{8(i-1)^2-1}\\&-4\sum_{i=2}^{l}\theta_{m}\sqrt{2(i-1)^2-\theta_{m}^2}\\&+8\sum_{i=2}^{l}(i-1)^2\arctan\frac{\sqrt{8(i-1)^2-\theta_{m}^2}}{\theta_{m}}\\&-8\sum_{i=2}^{l}(i-1)^2\arctan\sqrt{8(i-1)^2-1}\end{aligned} \quad (10)$$

The case of $p\to 0$ is equivalent to $l\to\infty$. Despite their formidable length and complexity, $A(m)$ and $B(m)$ are found to bear the following feature

$$\lim_{l\to\infty}\frac{A(m)}{B(m)}=\frac{1}{2} \quad (11)$$

and this concludes the proof of Theorem 1. More details on derivation of Eq. (11) can be found in Appendix C.

5 Extensions

5.1 3D analysis

The strategies used to accomplish the analysis in Section 4 can be extended to 3D data. The outer and inner boundaries of bucket i regions are illustrated in Fig. 10. The analysis should be based on the volume of relevant regions surrounding a cube $\mathbf{A}$ with side length δ. The bucket 1 region (Fig.10(a)) of $\mathbf{A}$ consists of the following components:

Table 3 Values of $\alpha(m+1)/\alpha(m)$ in 3D space under different values of m and l. Computed with Mathematica 6.0 based on formulae in Appendix B. Precision up to the 6th digit after decimal point.

Map	**Total Number of Histogram Buckets (l)**						
levels	2	4	8	16	32	64	256
m=1	0.531078	0.509177	0.502381	0.500598	0.50015	0.500038	0.500002
m=2	0.514551	0.504128	0.50102	0.500247	0.50006	0.500013	0.5
m=3	0.505114	0.500774	0.500051	0.499987	0.499991	0.501551	0.500004
m=4	0.498119	0.497695	0.499076	0.499717	0.499931	0.498428	0.5
m=5	0.490039	0.49337	0.496703	0.499313	0.499811	0.499966	0.499983
m=6	0.47651	0.485541	0.49586	0.498521	0.499586	0.499897	0.499897
m=7	0.448987	0.469814	0.48972	0.497032	0.499241	0.499793	0.500138
m=8	0.38559	0.435172	0.478726	0.494029	0.49848	0.499448	0.5

(1) quarter cylinders (green) with length δ and radius $p = \sqrt{3}\delta$;
(2) one-eighth of a sphere (red) with radius p;
(3) cuboids (white) with dimensions δ, δ, and p; and
(4) cube **A** itself, which is not shown in Fig. 10(a), but can be seen in Fig. 10(b).

There are eight pieces of each of the first two items and six pieces of item (3). The inner boundary (region **B**) of the bucket 2 region (Fig. 10(b)) consists of eight identical portions of a spherical surface centered at the opposite corner of **A** with radius p. Note that the projection of these regions on 2D are exactly those found in Fig. 4. Again, the shape of the region does not change with respect to bucket number i – we only need to change the radius from p to ip. The volume of the bucket i region can thus be expressed as

$$g(i) = \begin{cases} \frac{4}{3}\pi p^3 + 6p\delta^2 + 3\pi p^2\delta + \delta^3, & i = 1 \\ \frac{4}{3}\pi(ip)^3 + 6ip\delta^2 + 3\pi(ip)^2\delta + \delta^3 \\ \qquad -v(i,p,\delta), & i > 1 \end{cases}$$

where the first four items in both cases represent the volume of the four components listed above and $v(i,p,\delta)$ is that for the region formed by half of a spherical surface in Fig. 10(b). With $p = \sqrt{3}\delta$, the above equation becomes

$$g(i) = \begin{cases} \left(4\sqrt{3}\pi + 6\sqrt{3} + 9\pi + 1\right)\delta^3 & i = 1 \\ \left[4\sqrt{3}\pi i^3 + 6\sqrt{3}i + 9\pi i^2 + 1 - v(i,p)\right]\delta^3 & i > 1 \end{cases}$$

where $v(i,p) = 16V_{\mathbf{B}}$ and $V_{\mathbf{B}}$ is the volume of region **B** (see Appendix B for details).

We continue to develop formulae for the coverable regions $f(i,m)$ and non-covering factor $\alpha(m)$ as we do in Section 4.3 and Section 4.4. These formulae can be found in Appendix II of our technical report [37]. The complexity of such formulae hinders an analytical conclusion on the convergence of $\alpha(m+1)/\alpha(m)$ towards $\frac{1}{2}$. Fortunately, we are able to compute the numerical values of $\alpha(m+1)/\alpha(m)$ under a wide range of inputs.

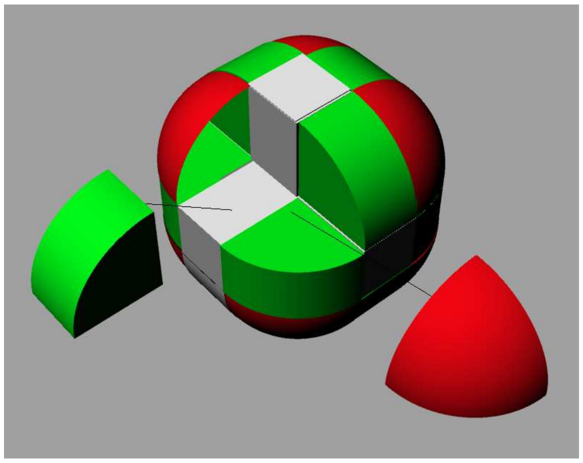
(a) Outer boundary of the bucket 1 region.

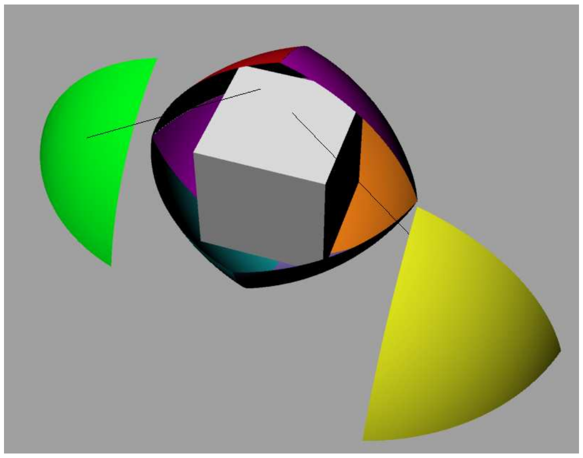
(b) Inner boundary of the bucket 2 region.

Fig. 10 Geometric structures of the bucket 1 and bucket 2 regions for 3D data.

These results (listed in Table 3) clearly show that it indeed converges to $\frac{1}{2}$. This technique can be extended to higher dimensions and we conjecture that Theorem 1 still holds true. However, since the real simulation data has up to three dimensions, our analysis stops at 3D.

$$f(i,m,s) = \begin{cases} \left[2\pi + 4\sqrt{2} + 1 - (8\sqrt{2}+4)\frac{1}{s^m} + \frac{4}{s^{2m}}\right]\delta^2 & i = 1, m \geq 1 \\ \left\{2\pi i^2 + 4\sqrt{2}i - (8\sqrt{2}i+4)\frac{1}{s^m} + \frac{4}{s^{2m}} - 8\left[(i-1)^2\left(\arctan\frac{\gamma'_m}{\theta'_m} - \frac{\pi}{4}\right) - \frac{1}{2}\theta'_m\left(\gamma'_m - \theta'_m\right)\right] + 1\right\}\delta^2 & i > 1, m > 1 \end{cases} \quad (12)$$

5.2 General Tiling Approach in Space Partitioning

In DT-SDH, the Quad-tree is built using a regular tiling [29] approach to partition the space, i.e., the subcells are of the same shape as the parent cell. In the previous analysis, for each node, we evenly cut each dimension by half, leading to 2^d partitions (child nodes) on the next level. However, in general, we could cut each dimension into $s > 2$ equal segments, giving rise to s^d equal-sized squares or cubes as in Fig. 11. In this section, we study how this affects the value of $\alpha(m)$.

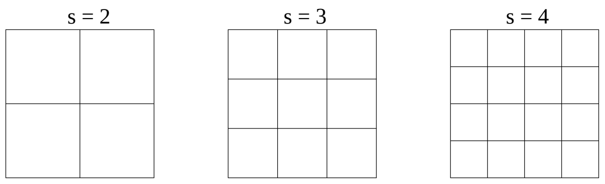

Fig. 11 Partitions of a 2D cell under different tiling factors.

First, the bucket i regions given by Eq. (3) are not affected. For the coverable regions, we incorporate the tiling factor s into the same reasoning as what we utilize to obtain Eq. (7). One exception here is the case of $m = 1, i \geq 2$: the approximate coverable region does not form a series of circles when $s > 2$, therefore Eq. (6) does not hold and this case should be handled in the same way as the case of $m > 1, i \geq 2$. Skipping the details, we get an improved version of Eq. (7) for $s > 2$ as Eq. (12), where $\theta'_m = \frac{1}{2} - \frac{1}{s^m}$ and $\gamma'_m = \sqrt{2(i-1)^2 - {\theta'_m}^2}$.

With Eq. (12) to describe the coverable regions, we can easily generate new equations for the covering factor as a function of m and s. By studying these functions, we get the following theorem.

Theorem 2 *With a tiling factor s ($s \in \mathbb{Z}^+$), the non-covering factors have the following property*

$$\lim_{l\to\infty} \frac{\alpha(m+1)}{\alpha(m)} = \frac{1}{s}.$$

Proof The techniques to achieve this proof are very similar to those for Theorem 1. See Appendix D for the details.

Theorem 2 is obviously a nicely-formatted extension of Theorem 1. Like Theorem 1, it is well supported by numerical results even under smaller values of l (details not shown in this paper). In Section 6, we will discuss the effects of s on the time complexity of DT-SDH.

6 Time Complexity of DT-SDH

With Theorem 2, we achieve the following analysis of the time complexity of DT-SDH as a function of the input size N.

Theorem 3 *If the data points are uniformly distributed in space, the time complexity of* DT-SDH *under a general tiling factor s is $\Theta\big(N^{\frac{2d-1}{d}}\big)$ where $d \in \{2,3\}$ is the number of dimensions of the data.*

Proof We derive the complexity of the algorithms by studying how the required time changes with the increase of system size N. Since the average number of particles in the leaf nodes is a constant β, one more level of tree will be built when N increases to s^dN. Therefore, we need to build a recurrence function that relates the running time under system size s^dN to that under N.

We first study the time spent on operation (i) (i.e., resolving the cell pairs). We denote this time as T_c. For a given bucket width p, the starting level DM_0 is fixed in DT-SDH. Assume there are I pairs of cells to be resolved on DM_0, the total number of cell pairs becomes Is^{2d} on the next level DM_1. According to Theorem 2, only one s-th of the I pairs on DM_0 will not be resolved, leaving Is^{2d-1} pairs to resolve on DM_1. On level DM_2, this number becomes $Is^{2d-1}\frac{1}{s}s^{2d} = Is^{2(2d-1)}$, and so on. Therefore, $T_c(N)$ can be expressed as the summation of numbers of cell pairs to resolve in all levels of the tree starting from DM_0:

$$\begin{aligned} T_c(N) &= I + Is^{2d-1} + Is^{2(2d-1)} + \cdots + Is^{n(2d-1)} \\ &= \frac{I\left[s^{(2d-1)(n+1)} - 1\right]}{s^{2d-1} - 1} \end{aligned} \quad (13)$$

where n is the total number of levels in the tree visited by the algorithm. The value of n increases by 1 when N increases to s^dN. Therefore, by revisiting Eq. (13), we have the following recurrence:

$$T_c(s^dN) = \frac{I\left[s^{(2d-1)(n+2)} - 1\right]}{s^{2d-1} - 1} = s^{2d-1}T_c(N) - o(1) \quad (14)$$

Based on the master theorem [8], the above recurrence gives

$$T_c(N) = \Theta\big(N^{\log_{s^d} s^{2d-1}}\big) = \Theta\big(N^{\frac{2d-1}{d}}\big).$$

Note that the above conclusion about operation (i) has nothing to do with the data distribution.

Now let us investigate the time complexity for performing operation (ii), i.e., pairwise distance calculation. Interestingly, we have similar results as in Eq. (14).

As shown in the derivation of Eq. (14), there are $Is^{n(2d-1)}$ pairs of leaf nodes to resolve, among which $Is^{n(2d-1)}\frac{1}{s} = Is^{n(2d-1)-1}$ will be unresolved and the pairwise distances of the particles in them need to be computed one by one. When system size increases from N to s^dN, the number of unresolved leaf node pairs (denoted as L) becomes $Is^{(n+1)(2d-1)-1}$. Thus, we get the following recurrence:

$$L(s^dN) = s^{2d-1}L(N),$$

which is essentially the same as Eq. (14) and we easily get

$$L(N) = \Theta\big(N^{\frac{2d-1}{d}}\big) \tag{15}$$

Note that $L(N)$ is the number of non-resolvable cell pairs. Due to the assumption of uniformly distributed data, the number of point-to-point distances in these cells also follows Eq. (15). In Section 6.1, we will show that this claim still holds true when the uniform assumption is relaxed.

Putting the above results about operations (i) and (ii) together, we conclude that **the time complexity of DT-SDH is $\Theta\big(N^{\frac{2d-1}{d}}\big)$**.

We have mentioned that our analysis is done based on an overestimation of the coverable regions on each density map, and the estimation error decreases as m increases. Relate this to Theorem 2, we have an underestimated non-covering factor α on each level. Since the estimation is more accurate on larger m, the real ratio of $\alpha(m+1)$ to $\alpha(m)$ can only be smaller than the one given by Theorem 2, making $\frac{1}{s}$ an upper bound. As a result, the complexity of the DT-SDH algorithm becomes $O\big(N^{\frac{2d-1}{d}}\big)$.

Note that the time complexity has nothing to do with the tiling factor s. In practice, we prefer smaller s values. Recall that the first map DM_0 should be the first level with cell size $\delta \le p/\sqrt{d}$. With a bushy tree as a result of large s value, the cell size decreases more dramatically and we could end up a DM_0 with cell size way smaller than $p/\sqrt{d}$, giving rise to more cells to resolve (Eq. (13)).

6.1 Effects of Spatial Distribution of Data Points

To prove Theorem 3, we need to transform Eq. (15) into one that describes the number of distance calculations in the unresolved leaf nodes. This is obviously true for uniformly distributed data, in which the expected number of points in a cell is proportional to the cell size. However, in this subsection, we will show that **Theorem 3 can be true even if we relax the assumption of uniformly distributed data points**.

A
a1
a2
a3
a4
B
b1
b2
b3
b4

Fig. 12 Two non-resolvable leaf cells are divided into four subcells when data size increases by a factor of s^d.

Let us consider any pair of non-resolvable cells $\mathcal{A}$ (with point count a) and $\mathcal{B}$ (with point count b) on the leaf level DM_k of the tree. Note that we cannot say $a = b$ (due to the non-uniform data distribution), and we expect to have $T_k = ab$ distances to compute between these two cells. When the system size increases from N to s^dN, we build another level of density map DM_{k+1}, in which $\mathcal{A}$ and $\mathcal{B}$ are both divided into s^d cells. Fig. 12 shows an example for $s = 2$ and $d = 2$. Let us denote the original number of data points in the subcells as a_i ($i \in \{1, 2, \cdots, s^d\}$) and b_j ($j \in \{1, 2, \cdots, s^d\}$). In other words, we have $a = \sum_{i=1}^{s^d} a_i$ and $b = \sum_{j=1}^{s^d} b_j$. When N increases to s^dN, a_i and b_j all get a s^d-fold increase and the expected number of distance calculations becomes

$$T_{k+1} = \sum_{i,j} P_{i,j} s^d a_i s^d b_j \tag{16}$$

where $P_{i,j}$ is a binary variable that tells whether subcells i and j are non-resolvable on DM_{k+1}. Without any assumptions, we only know that the average of $P_{i,j}$ over all combinations of i and j is $\frac{1}{s}$ (Theorem 2). For Theorem 3 to be true, we need to show that

$$T_{k+1} \le \frac{s^{2d}}{s} T_k = s^{2d-1}ab \tag{17}$$

6.1.1 Effects of a common point distribution

We first show that, if the distribution of data points is *cell-wise uniform* on density map DM_k, we can satisfy the condition specified in formula (17). Being cell-wise

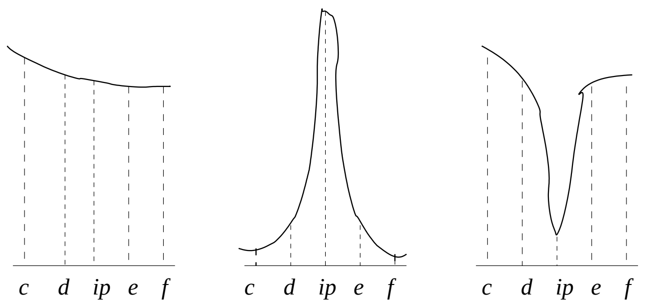

Fig. 13 Three cases of distribution of distances around the edge of buckets i and $i+1$, with the solid curves representing portions of the density function of the distances; $[c, d]$ and $[e, f]$ are examples of distance ranges of resolvable subcells. Those of the non-resolvable subcells are not shown. Line segments are not drawn on scale. For example, ip does not have to be the middle point of $[c, f]$ in practice.

uniform means that the data are uniformly distributed within each cell, i.e., we have

$$a_1 = a_2 = \cdots = a_{s^d} = \frac{a}{s^d}$$

and

$$b_1 = b_2 = \cdots = b_{s^d} = \frac{b}{s^d},$$

which easily leads to

$$T_{k+1} = \frac{1}{s} \sum P_{i,j} s^d a s^d b = s^{2d-1} ab.$$

Being a less constrained assumption than system-wise uniform distribution (which also requires $a = b$), the cell-wise uniform distribution is a safe assumption in many scientific domains. This is because components of natural systems are generally not compressed arbitrarily to form high-density clusters due to the existence of chemical bonds or inter-particle forces [1,26]. As a result, data points tend to spread out “evenly”, at least in a localized area. The water molecules is a good example of this. Note that we only need to make the assumption of cell-wise uniformity in the leaf nodes to make Theorem 3 true. In fact, we often found uniform regions on high-level tree nodes. For example, by studying the dataset illustrated in Fig. 1, we found that atoms are uniformly distributed in 61 out of 64 of the nodes on level 3 of the quad tree. Cell-wise uniformity is also a popular observation in many traditional spatiotemporal database applications [36].

6.1.2 More general conditions

A more general discussion on the necessary conditions of Theorem 3 would be helpful in identifying the limitations of DT-SDH. We believe that *skewed point distributions will affect the correctness of Theorem 3 only in rare cases.* Intuitively, a skewed point distribution can give rise to a skewed distance distribution. Revisiting Fig. 12 and Eq. (16), we can easily see that T_{k+1} is basically a sum of $s^{2d} a_i b_j$ weighted by the binary variable $P_{i,j}$, which has an average of $\frac{1}{s}$ according to Theorem 2. Therefore, the condition for Theorem 3 to hold true is that *there is no positive correlation between the occurrence of $P_{i,j} = 0$ and large values of $a_i b_j$.* In other words, as long as the peaks in the data distribution do not always co-exist with the non-resolvable cell pairs, Theorem 3 will not be harmed. We know $P_{i,j}$ is determined solely by the geometry of the cells and p. If we model the data placement as a regular stochastic process (e.g., Zipf, mixed Gaussian, ...) , the lack of correlation between $P_{i,j}$ and data distribution (on which the values of a_i, b_j depend) can be easily justified. An adversary can certainly generate cases to beat DT-SDH by adding more constraints to the data distribution. We will discuss that in Section 6.1.3.

Another way to describe the above condition is, as shown in the middle graph of Fig. 13, we cannot have high density of distances centering around (most or all of the) the bucket boundaries. Suppose two cells (e.g., $\mathcal{A}$ and $\mathcal{B}$ in Fig. 12) have a distance range $[c, f]$, which overlaps with buckets i and $i + 1$. With one more level of density map built, their subcell pairs could generate resolvable distance ranges such as $[c, d]$ and $[e, f]$ (because they do not contain ip – the boundary of the two buckets). It also generates non-resolvable distance ranges that contain ip. If the distribution of distances has high density around ip, most of the area under the density curve will fall into the non-resolvable ranges. On the contrary, if the density curve around ip is not a sharp peak (e.g., left graph in Fig. 13), we could have roughly equal amount of area under the resolvable and non-resolvable ranges. Or, in another extreme case (e.g., right graph of Fig. 13) where the density is very low around ip, most of the distances will be in the resolvable ranges.

Interestingly, there are easy remedies to the situation shown in the middle graph of Fig. 12. We can

(1) compute another SDH by moving the boundaries of all buckets to the left (or right) by $\frac{p}{2}$, or
(2) decrease the bucket width to γp where $0 < \gamma < 1.0$ and $\frac{1}{\gamma}$ is not an integer.

By both methods, we can generate a histogram that shows all the trends in the distance distribution (exactly what we need in a SDH) yet most of the distance calculations are avoided. In the second case, the SDH generated is of an even higher resolution. The technical details of designing such algorithms are beyond the scope of this paper.

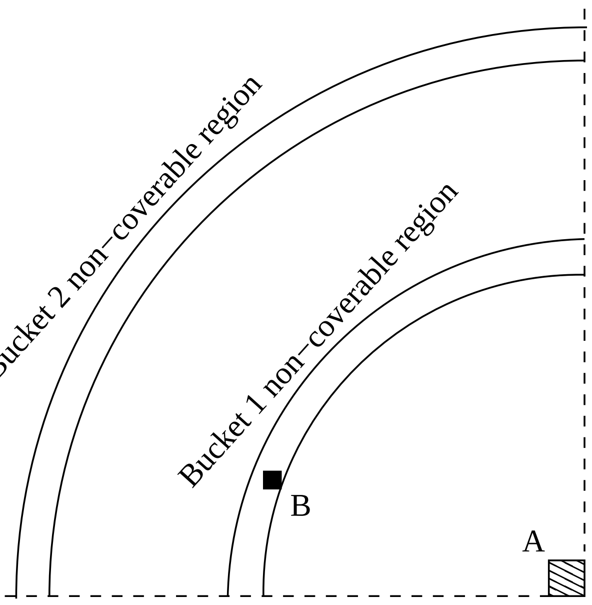

Fig. 14 A cell with a large number of data points in 2D space and its first two non-coverable regions (one the lowest level of the . The cell is denoted as cell A and non-coverable regions are presented by annuli (rings). Only one quarter of the regions are plotted.

6.1.3 Counterexamples to Theorem 3

In this subsection, we discuss data distribution patterns that serve as adversaries against DT-SDH. We have mentioned that Theorem 3 still holds true under cell-wise uniform distribution. Therefore, an adversary case would obviously involve tightly clustered data points. However, such clusters by themselves do not necessarily increase the time complexity of DT-SDH. To do that, additional conditions have to be satisfied.

Fig. 14 illustrates a high-density cluster A in 2D space. To study the impact of cluster A on Theorem 3, we have to consider the location of data points out of A. If the other data points spread out in the whole space, Theorem 3 would still be true as this is roughly the scenario of cell-wise uniform distribution. Therefore, it requires a large number of particles to be located in the non-coverable regions of A to make a "bad" case for DT-SDH. There can be two scenarios: 1) the other data points spread out in the non-coverable regions of A; 2) there are high-density clusters (e.g., B in Fig. 14) within the non-coverable regions. One thing to point out is: for the above scenarios to be effective adversaries, the points out of A must reside in a very narrow band. This is because the non-coverable regions shrink as the cells on the leaf nodes of the quad-tree get smaller (due to the increase of N, as shown by Theorem 1).

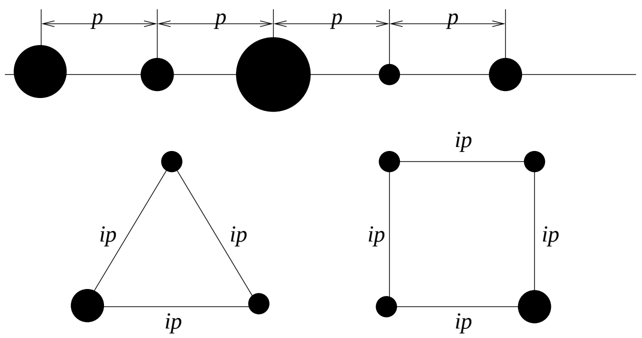

Fig. 15 Several patterns of particle spatial distribution that lead to large number of non-resolvable distances near the bucket boundaries. Each ball represents a cluster of particles. Line segments are not drawn to scale.

From the above discussions, we have shown the following two conditions of data distribution are required for constructing an adversary input for DT-SDH.

(1) high-density data clusters must exist;
(2) at least one pair of such clusters are in each others' non-coverable regions.

Some examples of such datasets are shown in Fig. 15, in which a large number of particles are in high-density clusters, and the distances between pairs of clusters equal to ip where i is a positive integer. In an extreme case (top graph in Fig. 15) where the distance between any pair of clusters is ip, the particles are organized in a linear pattern. Fortunately, real scientific data will not likely follow such data distributions because the particles in nature tend to spread out in space (instead of forming clumps with a particular distance from each other). Again, all cases mentioned here can be easily handled by the remedies introduced in Section 6.1.2.

6.2 SDH with Variable Bucket Width

So far, we have studied the performance of DT-SDH in computing a standard SDH in which all buckets are of the same width p. In this subsection, we extend our analysis to the processing of SDHs with variable bucket width. We denote p_i as the ending point of bucket i, i.e., bucket i covers the range $[p_{i-1}, p_i)$. Due to the variable bucket width, the results in Section 4 cannot be directly adopted to accomplish the analysis. Instead, we consider a variation of the DT-SDH algorithm (which we call DT-SDH') to compute the non-standard SDH and derive its time complexity. We then prove that the running time of DT-SDH is equivalent to that of DT-SDH'.

For a SDH with l buckets of variable size, DT-SDH' computes it in $l-1$ steps. In the ith step, we run DT-SDH to compute a SDH with only two buckets that are separated by p_i (i.e., the two buckets are $[0, p_i)$ and $[p_i, L_{max}]$). It is easy to see that the SDH of interest can be obtained from all such two-bucket SDHs. The only thing to point out is that, in each step of running DT-SDH, we choose the DM_0 based on the width of the smaller bucket (recall Eq. (2)).

Theorem 4 *The time complexity of running* DT-SDH' *for computing a non-standard SDH that divides the distance domain into two buckets is* $O\big(N^{\frac{2d-1}{d}} l\big)$ *where* $d \in \{2, 3\}$.

Proof The DT-SDH' runs DT-SDH for a total of $l - 1$ times, each time it computes a two-bucket SDH. To prove the theorem, it is sufficient to show that the time complexity of DT-SDH on computing any two-bucket SDH is $O\big(N^{\frac{2d-1}{d}}\big)$ – same as that for DT-SDH to computer a standard SDH. Without loss of generality, we denote the smaller one of the two bucket width as q and that of the other bucket as $r = L_{max} - q$. We can still use the techniques shown in Section 4 to analyze this, except we only need to consider two buckets $[0, q)$ and $[q, L_{max}]$. For the two buckets, we can then generate the area of the bucket regions $g(1)$ and $g(2)$, and that for the coverable regions $f(1, m)$ and $f(2, m)$. The formulae for the above area can be found in Appendix E. We then get the non-covering factor as

$$\alpha(m) = \frac{g(1) + g(2) - f(1, m) - f(2, m)}{g(1) + g(2)}$$

And the covering factor has the following feature

$$\frac{\alpha(m + 1)}{\alpha(m)} \leq \frac{1}{2}.$$

The above is similar to Theorem 1 and we easily conclude the proof by following the path we took to prove Theorem 3.

The following theorem gives the time complexity of DT-SDH on computing a non-standard SDH.

Theorem 5 *The time complexity of running* DT-SDH *for computing a SDH with variable bucket width is also* $O\big(N^{\frac{2d-1}{d}} l\big)$ *where* $d \in \{2, 3\}$.

Proof We achieve the proof by comparing the number of operations in the DT-SDH to that in DT-SDH'. Specifically, we have the following observations:

(1) type (ii) operations: if a pair of points fall into a pair of non-resolvable leaf cells in DT-SDH, they are also in the same non-resolvable leaf cells in DT-SDH';
(2) type (i) operations: for any pair of cells, if they are visited by DT-SDH for an attempt to resolve them, they are also visited by DT-SDH for the same purpose.

The above two facts show that the time spent by DT-SDH is no more than that by DT-SDH' to process the same dataset, and this concludes the proof.

7 Empirical Evaluations

7.1 Experimental Setup

We have implemented the DT-SDH algorithms using the C programming language and tested it with synthetic and real datasets. The experiments were run in an Apple Mac Pro workstation with two dual-core Intel Xeon 2.66GHz CPUs, and 8GB of physical memory. The operating system was OS X 10.5 Leopard.

The datasets used in our experiments include three groups of synthetic ones and data from real simulations. Among the synthetic data groups, one was generated following a uniform distribution of data points, one following a Zipf distribution with various orders, and one from a mixed-Gaussian distribution. All point coordinates in the synthetic datasets are rendered in a 3D cube whose side length is 25,000 units. For the Zipf-based datasets, we divided the entire data space into a large number of small blocks (i.e., cubes with side length 5 to 50) and each small cube was assigned a random rank. Given two cubes with ranks i and j, the expected number of data points are of ratio $j^{\alpha} : i^{\alpha}$ where $\alpha \geq 1.0$ is the *order* of the Zipf distribution. The well-known fact is that, even with order 1.0, a Zipf distribution brings high level of skewness in the data. We also generated test data using the mixed Gaussian model. Specifically, the data points are rendered from 3 – 5 normal distributions with a fixed standard deviation and means randomly chosen within a 2D simulation space. Each normal distribution carries the same weight, and we assume there is no correlation among the two dimensions. We used a series of C libraries provided by the randlib [4] package to generate relevant random numbers.

The other dataset is generated from a real molecular dynamics study to simulate a bilayer membrane lipid system in NaCl and KCl solutions, as illustrated in Fig. 1. The original dataset records the coordinates of 286,000 atoms over 10,000 time instances (data in each time step is called a *frame*). In order to make the experiments comparable to those using synthetic data, we randomly choose and duplicate atoms in this dataset to reach different dataset sizes N. Specifically, we combine the data from consecutive frames to create datasets with size greater than 286,000.

[4] http://randlib.sourceforge.net/

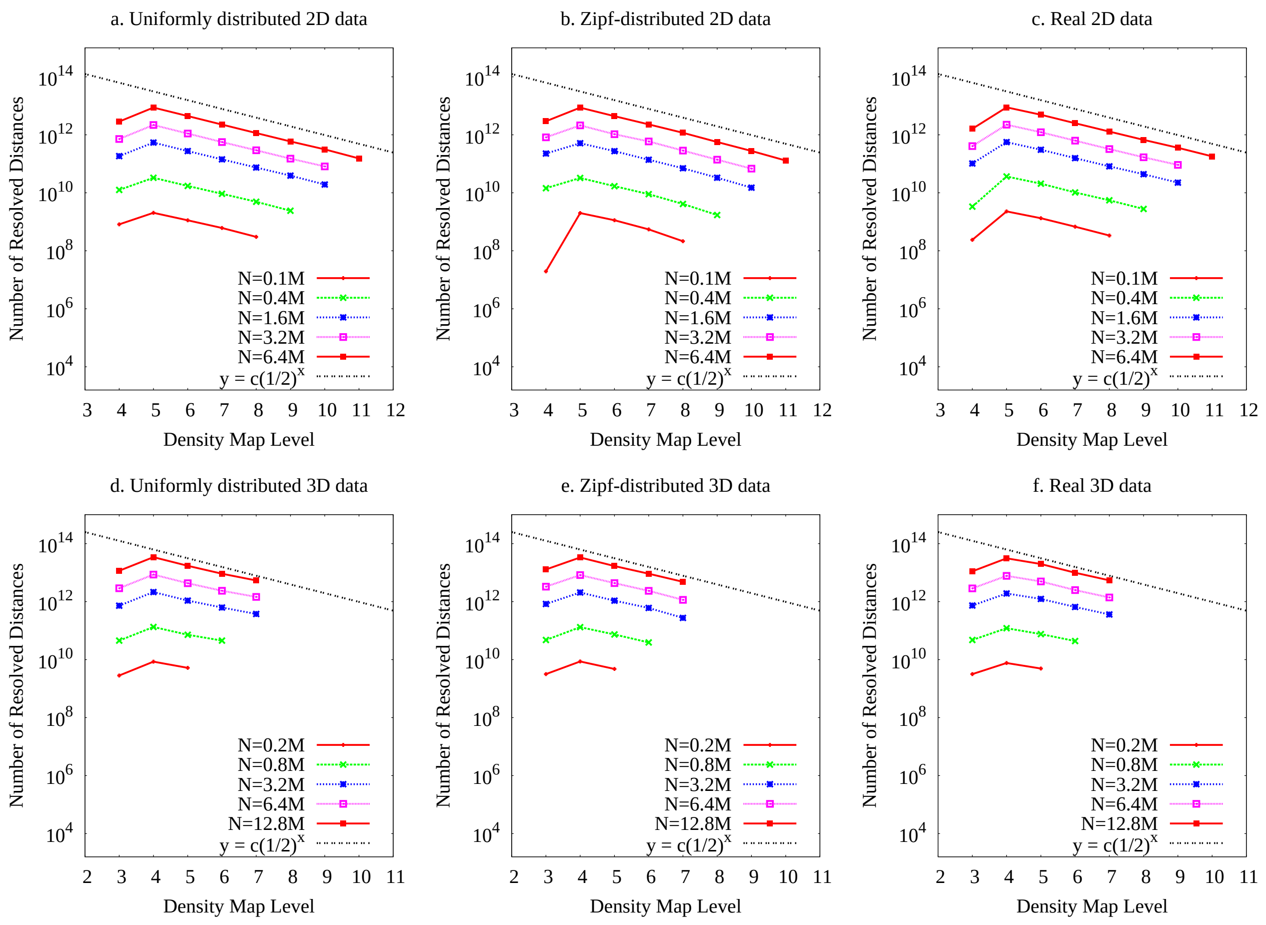

Fig. 16 Number of distances resolved on different levels of the tree.

All experiments were run under a series of N values ranging from 100,000 to 25,600,000. In the following text, we report the results of three lines of experiments.

7.2 Model Verification

The objective of this set of experiments is to evaluate the correctness of our basic analytical model, which gives Theorem 1 as the foundation of complexity analysis. Instead of verifying the values of $\alpha(m+1)/\alpha(m)$ listed in Tables 2 and 3, we focus on the number of distances in the non-resolvable cells under different m values to study how data distribution (especially the skewed ones) affects the effectiveness of our model. Ideally, the number of unresolved distances should follow the same pattern as described in Theorem 1 - it should decrease by half every time m increases by 1.

Fig. 16 shows the absolute number of resolved distances (plotted on a logarithmic scale) achieved. Each line represents one experiment on a dataset of a particular size. For all experiments, we can see that the line starts from a small value and then reaches the highest value on the following level. The first value in each line reflects those distances resolved on DM_0 - it is small because it only contains those intra-cell distances that resolve into bucket 1. Starting from DM_1, the values drop at a rate that is close to $\frac{1}{2}$ – this trend can be easily seen by comparing the slopes of the data lines to that of a standard function $y = c\left(\frac{1}{2}\right)^x$. One thing to point out is: the slopes of some of the data lines in Fig.16 (e.g., the top lines in all 3D experiments) are even slightly smaller than the standard curve. This is a positive result which indicates that the distances are consumed in a higher rate than what we expect from our model. To better interpret the experimental results, we need to see from an opposite angle by showing how many distances are left unresolved on each level.

For the same experiments, Fig. 17 plots the percentage of unresolved distances on a logarithmic scale. Again, each line starts by the reading of DM_0 and we draw a standard line with slope $-\frac{1}{2}$ to indicate the expected trend given by Theorem 1. It is easy to see that the distances are resolved at a rate close to $\frac{1}{2}$. The only

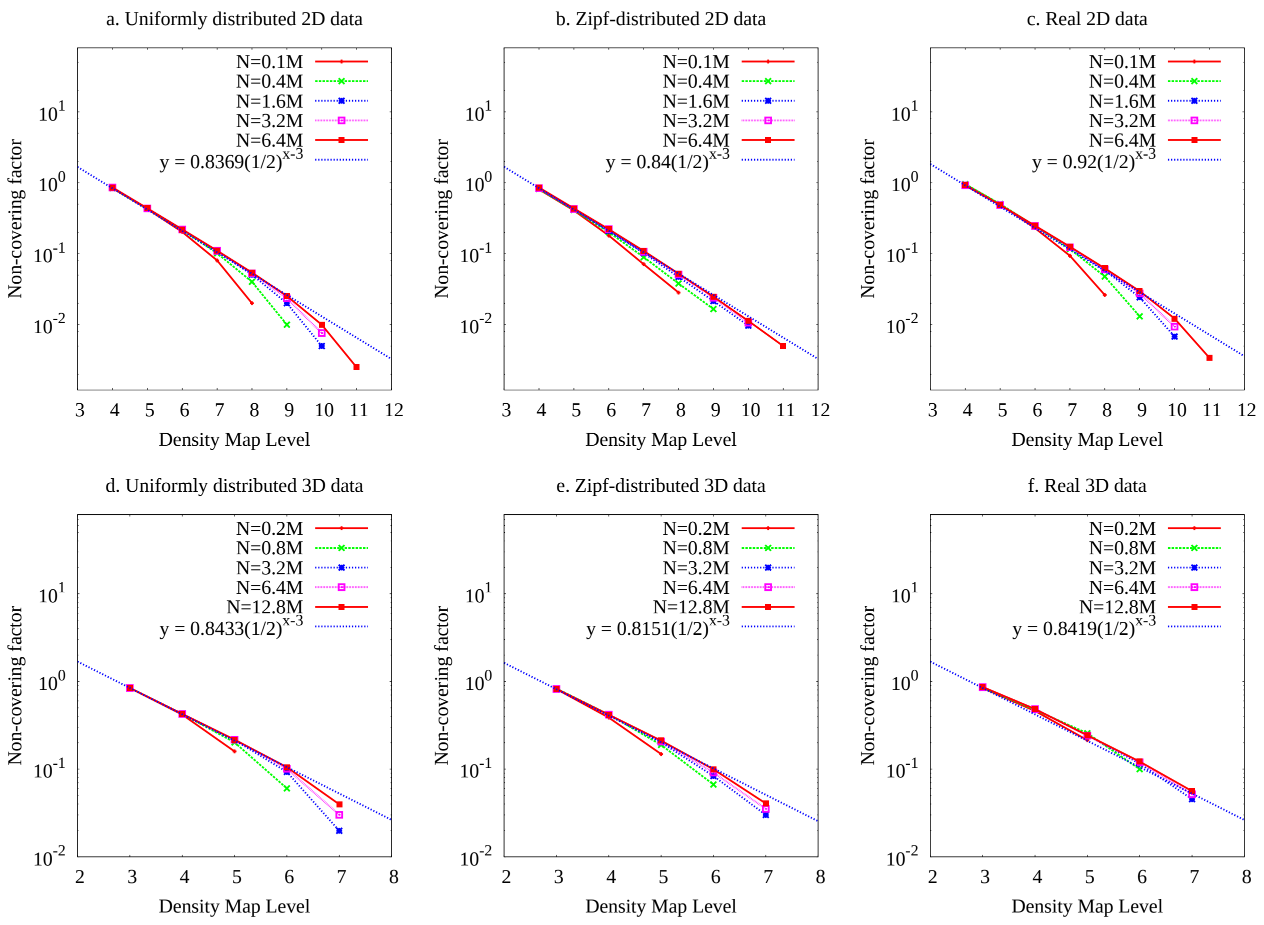

Fig. 17 Non-covering factors upon visiting different levels of the tree. Here the factor is calculated as the ratio of number of unresolved distances to total number of distances after visiting m levels in the tree.

exceptions appear in the real 3D simulation data experiment (Fig. 17f) where the number of distances decrease at a slightly slower rate on the middle levels. But the final values all ended up below the standard line. Clearly, this is in conformity with Theorem 1, which says half of the uncovered area will be covered by going one level down the tree. In fact, a majority of the plotted values are below the corresponding standard lines, supporting our claim that Theorem 1 is actually a lower bound of the expected performance. The important information here is that the number of resolved distances shows the same trend for all datasets, indicating the robustness of our model. The skewed Zipf point distribution does not at all cause degraded performance. In fact, we found that, among the three datasets, it always **took the least amount of time for DT-SDH to process the Zipf dataset**. Here we hold the discussions on the effects of data skewness on running time till Section 7.4 where the results of more skewed datasets (Zipf, mixed-Gaussian) will be reported.

7.3 Efficiency of DT-SDH

The main purpose of this experiment is to verify the time complexity of DT-SDH. In Fig. 18, the running time of our algorithm are plotted against the size of 2D experimental datasets. Fig. 18a shows the results of uniformly distributed data and Fig. 18b for those following the Zipf distribution, and Fig. 18c for the real simulation data. Both the running time and data size are plotted on logarithmic scales therefore the slopes of the lines reflect the time complexity of the algorithms. For comparisons, we draw an identical dotted line in each graph with a slope of 1.5. Each point in the graphs shows the result of one single run of DT-SDH as the long running time under large N prohibits having multiple runs. However, we did run multiple experiments with different random seeds for the cases of smaller N and observed very little variances in running time.

The brute-force approach (‘Dist’) always shows an exact quadratic running time (i.e., the slope of the line is 2). The other lines (with spots) represent experiments

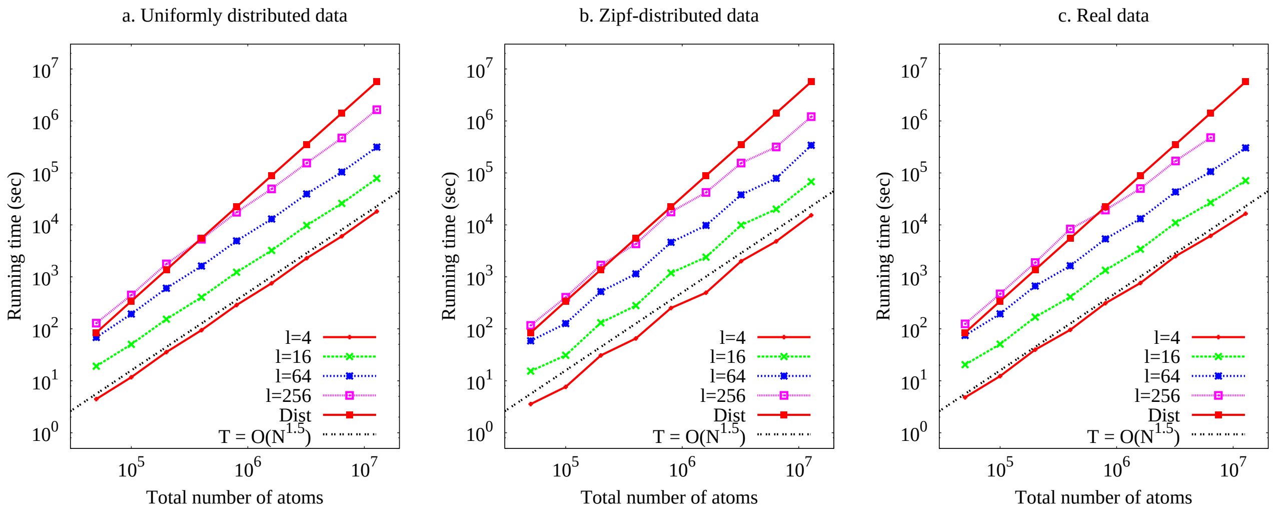

Fig. 18 Running time of the DT-SDH algorithm with 2D data.

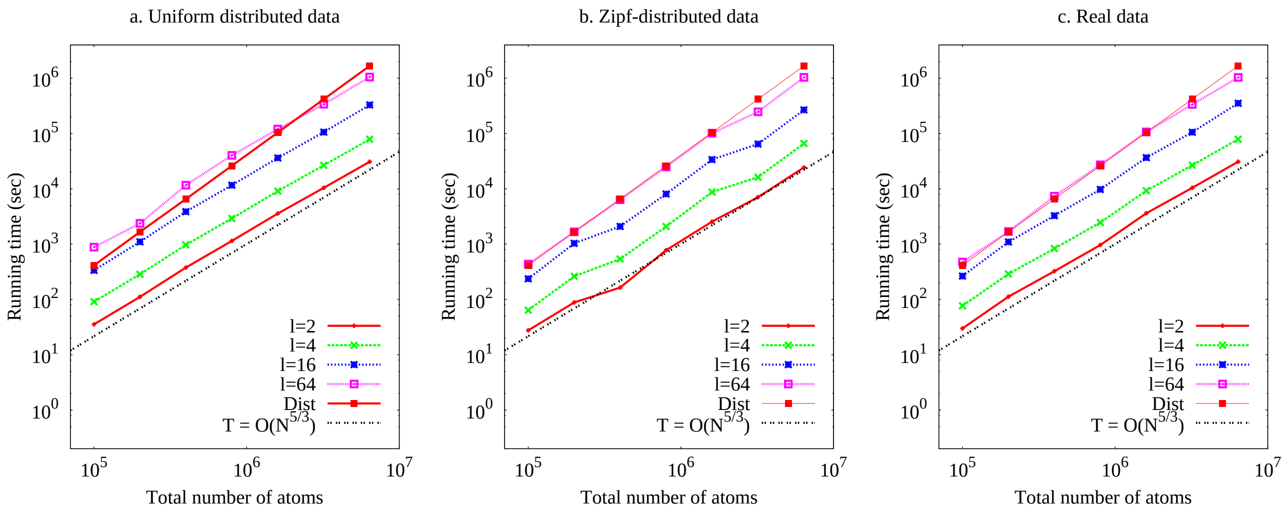

Fig. 19 Running time of the DT-SDH algorithm with 3D data.

using our algorithm under different bucket numbers l. Clearly, the running time of our algorithm grows less dramatically - they all have a slope of about 1.5. When bucket size decreases, it takes more time to run our algorithm, although the time complexity is still $\Theta(N^{1.5})$. The cases of large bucket numbers ('$l = 256$') are worth some attention: the running time is similar to that of the brute-force approach when N is small. As N increases, the slope of the line changes to around 1.5. The reason for this is: when N is small, we have a tree with very few levels; when the query comes with a very small bucket size p, we end up starting DT-SDH from the leaf level of the tree and have to essentially calculate most or all distances. However, the same query will get the chance to resolve more cells when the tree becomes taller, as a result of larger N. Again, the actual running time for the skewed dataset is always shorter than that for the uniform dataset with the same size. This can be seen by the relative positions of colored lines to the '$T = O(N^{1.5})$' line. The results of the real dataset are almost the same as those for the uniform data.

We have similar results for 3D data (Fig. 19): the corresponding lines for DT-SDH have slopes that are very close to $\frac{5}{3}$, confirming our asymptotic analysis. Again, the cases for large l values are worth more discussions. For '$l = 64$', the running time grows quadratically till N becomes fairly large (1,600,000) and then the slope of the line changes to $\frac{5}{3}$. One thing to notice is that the slope of the last segment of '$l = 64$' in Fig. 19b is almost 2. This does not mean the time complexity is going back to quadratic. In fact, it has something to do with the zigzag pattern of running time change in the Zipf data: for three consecutive doubling N values (i.e., a 8-fold increase), the running time increases by

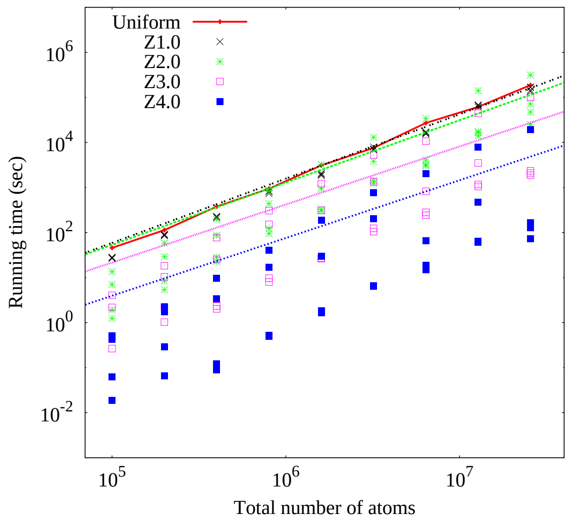

(a) Results of block size 50.

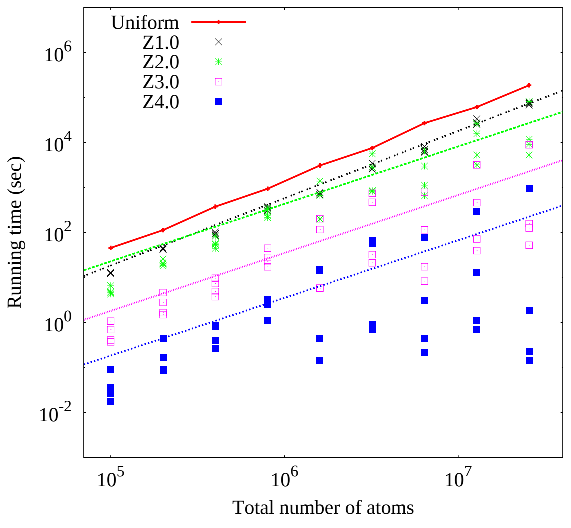

(b) Results of block size 5.

Fig. 20 Running time of DT-SDH with Zipf input data under different orders. Both left and right graphs are plotted on the exact same scale for easy comparisons.

2, 4, and 4 times, which still gives a $2 \times 4 \times 4 = 32$ fold increase in total running time (instead of a 64-fold increase in a quadratic algorithm).

7.4 Effects of Skewed Data Distribution

To further test the effects of skewed datasets on the performance of DT-SDH, we run 2D experiments using data generated from Zipf distribution of different orders and the mixed Gaussian distributions with different standard deviations (SD). By increasing the order of Zipf or the SD of the mixed Gaussian, we are supposed to generate more skewed datasets as more points will be concentrated on small regions. In these experiments, we computed a histogram with bucket width 4419.0. [5] Four random seeds were used to generate data of different sizes ranging from 100000 to 25600000. Thus, for a particular N (under one Zipf order) we tested the algorithm with four datasets.

The results of the Zipf datasets are shown in Fig. 20, in which both data size and running time are plotted on logarithmic scales. The same experiments were run under two block sizes (50 and 5), representing two levels of "tightness" of the clusters in the data. We plot the running time of each run of DT-SDH as a dot. By comparing the Zipf data to the uniform, we can easily see that, at most of the time, the time spent to compute SDH in a Zipf dataset is less than that for the uniform dataset. The only exceptions are for datasets generated from a particular random seed under Zipf order 2.0 and block size 50 (Fig. 20(a)). We will scrutinize those cases later. When the Zipf order increases from 1.0 to 4.0, we can observe two trends:

(1) the running time decreases. In some cases of Zipf order 4.0, we can see a decrease of up to 4 orders of magnitude; and
(2) the variances of the running time among the four random datasets (under the same N) increase.

The first observation directly shows that data skewness has positive effects on the efficiency of DT-SDH. The large variances for the high-order Zipf cases indicate that the position of clusters plays a role in determining running time, given the fact that all four runs used data with the exact same "skewness". We also used the Gnuplot function-fitting tools to derive functions that describe the relationship between N and the running time for all Zipf orders. Specifically, we fit the dots into functions of the form $T = aN^b + c$ and such functions are drawn in the same color as that of their corresponding dots in Fig. 20. The positions of such lines in Fig. 20 show the above trends clearly. In Fig. 20(a), the function of Zipf order 1.0 (e.g., 'Z1.0') has a similar slope (i.e, 1.42) to that of the uniform data (e.g., 1.5) while the slopes of higher-order Zipf datasets are in the range of $(1.27, 1.28)$. This shows that the time complexity of DT-SDH tends to decrease when more skewed data are input. One thing to point out is: non-linear function fitting is not exact science and the details of the function-fitting methods used by Gnuplot are not re-

[5] This is exactly the diagonal of cells on the 4th level of the tree. We chose a relatively large p to save the total experimental time. We believe it is sufficient to show the trends.

vealed. Therefore, the parameter b in the fitted functions (i.e., slopes of the lines) can only be regarded as an indication of the algorithm's time complexity.

By decreasing the block size of the Zipf distribution, we will generate more "skewed " data. As a result (see Fig. 20(b)), we recorded shorter running times for almost all experimental runs as compared to those with block size 50. This can be easily captured by comparing the locations of corresponding dots and fitted functions in Fig. 20(b) and Fig. 20(a). While the line slopes are still in the neighborhood of 1.28 for Zipf data with orders 2.0, 3.0, and 4.0, the a parameters of the fitted functions are of much smaller values than in Fig, 20(a). In the case of Zipf with orders 3.0 and 4.0, a difference of more than one order of magnitude can be observed.

Fig. 21 shows the running time with the mixed-Gaussian data. The results are very similar to those of the Zipf data. When the SD decreases, the skewness of data also increases, and the running time decreases accordingly. In the extreme case of $SD = 50$, most datasets are processed within a fraction of a second (it went as low as 10^{-5} seconds). The variance of the running time caused by the four runs of each experiment also increases as SD becomes smaller. The fitted functions of all mixed-Gaussian experiments have slopes in the range of $[1.22, 1.30]$, which is still significantly smaller than the 1.5 of the uniform data results. The data related to Fig. 21(a) were generated from a mixture of three Gaussian distributions while those in Fig. 21(b) mixture of five. The general trend is that the running time of experiments with the same parameters N and SD increases in Fig. 21(b). Clearly, as the number of high-density data cluster increases (since each each Gaussian gives rise to one cluster), the data becomes less skewed, and running time increases. In this set of experiments, we have seen no cases in which the mixed-Gaussian data required longer time to process than the corresponding uniform data. We believe the above results are another set of evidence that shows the benefits of skewed datasets increase as the data becomes more skewed.

In summary, our experiments show that DT-SDH is generally more efficient in processing skewed data. The more skewed the data is, the shorter the processing time is. In an extreme case in Fig. 20(b), it takes only a fraction of a second to process a dataset with 25.6 million points. The only "bad" cases (Fig. 20(a)) are caused by one random seed in generating Zipf data with order 2.0. By looking deeply into the actual data distribution in such cases, we found that there are 4 large clusters (ranked 3, 6, 7, and 8) fall into the non-coverable regions of the rank 1 cluster. As a result, distances are resolved in a lower rate than in the uniform data. On contrary to that, distances are consumed quickly in all other skewed datasets - we even observed several cases (for Zipf order 4.0) in which 100% of the distances are resolved. In addition to the absolute running time, we also believe the time complexity of DT-SDH can be lower than what expect from Theorem 3 when the input data is very skewed.

8 Conclusions and Future Work

In this paper, we present analytical results related to the time complexity of a Quad tree-based algorithm for computing many statistical measures of large-scale spatial data. The spatial distance histogram is one salient example of such measures. Being the main building blocks of high-level analytics in a wide range of computational science fields, such histograms are of great importance in domain-specific hypothesis testing and scientific discovery. This paper focuses on the methodology we adopt to accomplish the analysis: we transform the problem into quantifying the area of certain regions in space such that geometric modeling can be used to generate rigorous results. Our analysis shows that the algorithm has complexity $O(N^{\frac{3}{2}})$ for 2D data and $O(N^{\frac{5}{3}})$ for 3D data. To the best of our knowledge, this is the best result so far in the computation of exact SDH. We also show that the conclusion holds true under a wide range of spatial distributions of data points in the dataset, improving on previous conjectures that only consider uniformly distributed data.

Immediate future work in this area involves more explorations on the approximate algorithm. While experimental results show very promising tradeoffs of running time and query error, probabilistic models have to be developed to study tight bounds of the error. Based on such models, more efficient and accurate heuristics for distributing distances into overlapping buckets can be designed. Eventually, the extension of our methodology to the computation of higher order n-body correlation functions will depend on our explorations on the lower-order functions. Another direction is to compute the SDH in consecutive frames efficiently by taking advantage of the temporal locality of data points.

Acknowledgements The project described was supported by Award Number R01GM086707 from the National Institute Of General Medical Sciences (NIGMS) at the National Institutes of Health (NIH). The content is solely the responsibility of the authors and does not necessarily represent the official views of NIGMS or NIH.

The authors would also like to thank Dr. Sagar Pandit in the Department of Physics at the University of South Florida for discussions on general particle simulation problems.

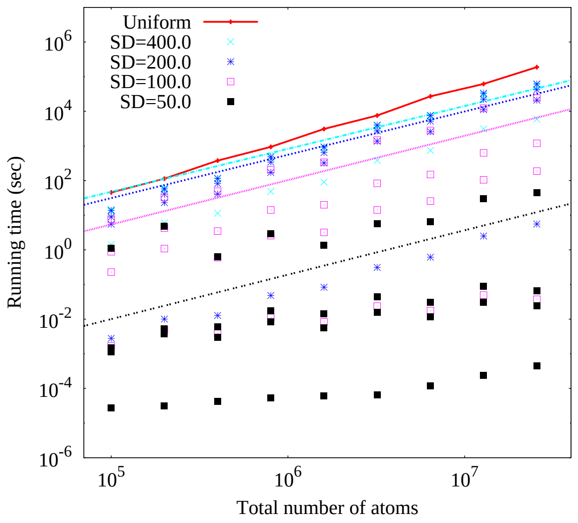

(a) Results of data with three clusters.

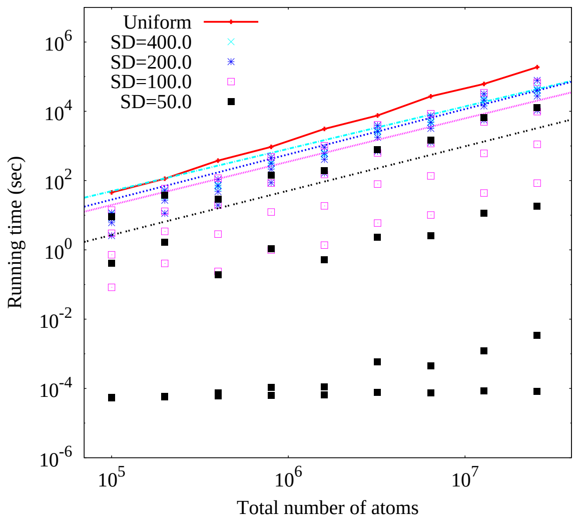

(b) Results of data with five clusters.

Fig. 21 Running time of DT-SDH with mixed-Gaussian data under different standard deviations. Both left and right graphs are plotted on the exact same scale for easy comparisons.

References

1. M. Allen. *Introduction to Molecular Dynamics Simulation*. John von Neumann Institute of Computing, NIC Seris, vol. 23, 2003.
2. M. P. Allen and D. J. Tildesley. *Computer Simulations of Liquids*. Clarendon Press, Oxford, 1987.
3. M. Arya, W. F. Cody, C. Faloutsos, J. Richardson, and A. Toya. QBISM: Extending a DBMS to Support 3D Medical Images. In *ICDE*, pages 314–325, 1994.
4. M. Bamdad, S. Alavi, B. Najafi, and E. Keshavarzi. A new expression for radial distribution function and infinite shear modulus of lennard-jones fluids. *Chem. Phys.*, 325:554–562, 2006.
5. J. Barnes and P. Hut. A Hierarchical O(N log N) Force-Calculation Algorithm. *Nature*, 324(4):446–449, 1986.
6. P. G. Brown. Overview of scidb: large scale array storage, processing and analysis. In *SIGMOD Conference*, pages 963–968, 2010.
7. P. B. Callahan and S. R. Kosaraju. A decomposition of multidimensional point sets with applications to k-nearest-neighbors and n-body potential fields. *Journal of ACM*, 42(1):67–90, 1995.
8. T. H. Cormen, C. E. Leiserson, R. L. Rivest, and C. Stein. *Introduction to Algorithms*, pages 73–75. MIT Press and McGraw-Hill, second edition, 2001.
9. I. Csabai, M. Trencseni, L. Dobos, P. Jozsa, G. Herczegh, N. Purger, T. Budavari, and A. S. Szalay. Spatial Indexing of Large Multidimensional Databases. In *Proceedings of the 3rd Biennial Conference on Innovative Data Systems Resarch (CIDR)*, pages 207–218, 2007.
10. M. Y. Eltabakh, M. Ouzzani, and W. G. Aref. BDBMS - A Database Management System for Biological Data. In *Proceedings of the 3rd Biennial Conference on Innovative Data Systems Resarch (CIDR)*, pages 196–206, 2007.
11. M. Feig, M. Abdullah, L. Johnsson, and B. M. Pettitt. Large Scale Distributed Data Repository: Design of a Molecular Dynamics Trajectory Database. *Future Generation Computer Systems*, 16(1):101–110, January 1999.
12. A. Filipponi. The radial distribution function probed by X–ray absorption spectroscopy. *J. Phys.: Condens. Matter*, 6:8415–8427, 1994.
13. G. Finocchiaro, T. Wang, R. Hoffmann, A. Gonzalez, and R. Wade. DSMM: a Database of Simulated Molecular Motions. *Nucleic Acids Research*, 31(1):456–457, 2003.
14. D. Frenkel and B. Smit. *Understanding Molecular Simulation: From Algorithm to Applications*, volume 1 of *Computational Science Series*. Academic Press, 2002.
15. D. Gawlick, D. Lenkov, A. Yalamanchi, and L. Chernobrod. Applications for expression data in relational database system. In *ICDE*, pages 609–620, 2004.
16. A. G. Gray and A. W. Moore. N-body problems in statistical learning. In *Advances in Neural Information Processing Systems (NIPS)*, pages 521–527. MIT Press, 2000.
17. J. Gray, D. Liu, M. Nieto-Santisteban, A. Szalay, D. DeWitt, and G. Heber. Scientific Data Management in the Coming Decade. *SIGMOD Record*, 34(4):34–41, December 2005.
18. L. Greengard and V. Rokhlin. A Fast Algorithm for Particle Simulations . *Journal of Computational Physics*, 135(12):280–292, 1987.
19. G. Heber and J. Gray. Supporting Finite Element Analysis with a Relational Database Backend. Part I:: There is Life Beyond Files. Technical Report MSR-TR-2005-49, Microsoft Research, 2005.
20. B. Hess, C. Kutzner, D. van der Spoel, and E. Lindahl. GROMACS 4: Algorithms for Highly Efficient, Load-Balanced, and Scalable Molecular Simulation. *Journal of Chemical Theory and Computation*, 4(3):435–447, March 2008.
21. B. Howe, D. Maier, and L. Bright. Smoothing the ROI Curve for Scientific Data Management Applications. In *CIDR*, pages 185–195, 2007.
22. S. Klasky, B. Ludaescher, and M. Parashar. The Center for Plasma Edge Simulation Workflow Requirements. In *EEE Workshop on Workflow and Data Flow for Scientific Applications (SciFlow'06)*, pages 73–73, 1991.
23. L. Krishnamurthy, J. Nadeau, G. Ozsoyoglu, M. Ozsoyoglu, G. Schaeffer, M. Tasan, and W. Xu. Pathways database system: an integrated system for biological pathways. *Bioinformatics*, 19(8):930–937, August 2003.

24. X. Ma, M. Winslett, J. Norris, X. Jiao, and R. Fiedler. Godiva: Lightweight data management for scientific visualization applications. In *ICDE*, pages 732–744, 2004.
25. A. W. Moore, A. J. Connolly, C. Genovese, A. Gray, L. Grone, N. K. II, R. C. Nichol, J. Schneider, A. S. Szalay, I. Szapudi, and L. Wasserman. *Mining the Sky*, volume 2001 of *ESO Astrophysics Symposia*, chapter Fast Algorithms and Efficient Statistics: N-Point Correlation Functions, pages 71–82. Srpinger/Heidelberg, February 2006.
26. A. Omeltchenko, T. J. Campbell, R. K. Kalia, X. Liu, A. Nakano, and P. Vashishta. Scalable I/O of Large-Scale Molecular Dynamics Simulations: A Data-Compression Algorithm. *Computer Physics Communications*, 131:78–85, 2000.
27. J. A. Orenstein. Multidimensional Tries used for Associative Searching. *Information Processing Letters*, 14(4):150–157, 1982.
28. J. M. Patel. The Role of Declarative Querying in Bioinformatics. *OMICS: A Journal of Integrative Biology*, 7(1):89–91, 2003.
29. H. Samet. The quadtree and related hierarchical data structures. *ACM Comput. Surv.*, 16(2):187–260, 1984.
30. V. Springel, S. D. M. White, A. Jenkins, C. S. Frenk, N. Yoshida, L. Gao, J. Navarro, R. Thacker, D. Croton, J. Helly, J. A. Peacock, S. Cole, P. Thomas, H. Couchman, A. Evrard, J. Colberg, and F. Pearce. Simulations of the Formation, Evolution and Clustering of Galaxies and Quasars. *Nature*, 435:629–636, June 2005.
31. J. L. Stark and F. Murtagh. *Astronomical Image and Data Analysis*. Springer, 2002.
32. M. Stonebraker, S. Madden, D. J. Abadi, S. Harizopoulos, N. Hachem, and P. Helland. The End of an Architectural Era (It's Time for a Complete Rewrite). In *VLDB*, pages 1150–1160, 2007.
33. A. S. Szalay, J. Gray, A. Thakar, P. Z. Kunszt, T. Malik, J. Raddick, C. Stoughton, and J. vandenBerg. The SDSS Skyserver: Public Access to the Sloan Digital Sky Server Data. In *Proceedings of International Conference on Management of Data (SIGMOD)*, pages 570–581, 2002.
34. I. Szapudi. A New Method for Calculating Counts in Cells. *The Astrophysical Journal*, 493(1):39–51, 1998.
35. I. Szapudi, S. Colombi, and F. Bernardeau. Cosmic Statistics of Statistics. *Monthly Notes of the Royal Astronomical Society*, 310(2):428–444, 1999.
36. Y. Tao, J. Sun, and D. Papadias. Analysis of predictive spatio-temporal queries. *ACM Trans. Database Syst.*, 28(4):295–336, 2003.
37. Y.-C. Tu, S. Chen, and S. Pandit. Computing Spatial Distance Histograms Efficiently in Scientific Databases. Technical Report CSE/08-103, http://www.cse.usf.edu/~ytu/pub/tr/pdh.pdf, Department of Computer Science and Engineering, University of South Florida, 2008.
38. Y.-C. Tu, S. Chen, and S. Pandit. Computing Distance Histograms Efficiently in Scientific Databases. In *Proceedings of International Conference on Data Engineering (ICDE)*, pages 796–807, March 2009.
39. C. Türker, F. Akal, D. Joho, and R. Schlapbach. B-fabric: An open source life sciences data management system. In *SSDBM*, pages 185–190, 2009.
40. W. Xu, S. Ozer, and R. R. Gutell. Covariant Evolutionary Event Analysis for Base Interaction Prediction Using a Relational Database Management System for RNA. In *SSDBM*, pages 200–216, 2009.

Appendix

A The area of coverable region for $m > 1$ and $i \geq 2$

First, we get the magnitude of angle BCD by

$$\begin{aligned}\angle BCD &= \angle DCE - \angle FCE = \arctan\frac{DE}{EC} - \frac{\pi}{4}\\ &= \arctan\frac{\sqrt{[(i-1)p]^2 - \left(\frac{\delta}{2} - \frac{\delta}{2^m}\right)^2}}{\frac{\delta}{2} - \frac{\delta}{2^m}} - \frac{\pi}{4}\end{aligned}$$

The area of the sector $\widehat{BDC}$ is $\frac{1}{2}[(i-1)p]^2\angle BCD$, and the area of the region $\widehat{BDGF}$ is

$$\begin{aligned}S_{\widehat{BDGF}} &= S_{\widehat{BDC}} - S_{\triangle DHC} - S_{\triangle FGH}\\ &= \frac{1}{2}[(i-1)p]^2\angle BCD - \frac{1}{2}EC(DE - HE) - \frac{\delta^2}{8}\\ &= \frac{1}{2}[(i-1)p]^2\left[\arctan\frac{\sqrt{[(i-1)p]^2 - \delta^2\theta_m^2}}{\delta\theta_m} - \frac{\pi}{4}\right]\\ &\quad -\frac{\delta}{2}\theta_m\left[\sqrt{[(i-1)p]^2 - (\delta\theta_m)^2} - \delta\theta_m\right] - \frac{\delta^2}{8}\end{aligned}$$

Finally, we get the area of the coverable region for $i \geq 2, m > 1$ as

$$\begin{aligned}S_{A'} &= S_{out}(i) - 8S_{\widehat{BDGF}} - S_A\\ &= \pi(ip)^2 + 4ip\left(\delta - \frac{2\delta}{2^m}\right) + \left(\delta - \frac{2\delta}{2^m}\right)^2\\ &\quad - 4[(i-1)p]^2\left[\arctan\frac{\sqrt{[(i-1)p]^2 - \delta^2\theta_m^2}}{\delta\theta_m} - \frac{\pi}{4}\right]\\ &\quad + 4\delta\theta_m\left[\sqrt{[(i-1)p]^2 - (\delta\theta_m)^2} - \delta\theta_m\right] \qquad (18)\end{aligned}$$

B Volume of region B in 3D case

$$\begin{aligned}V_{\mathbf{B}} &= \iint_{\mathbf{B}} dxdy\int_{\delta/2}^{\sqrt{p^2-x^2-y^2}} dz\\ &= \iint_{\mathbf{B}}\left(\sqrt{p^2 - x^2 - y^2} - \frac{\delta}{2}\right)dxdy\\ &= \int_a^{\frac{\pi}{4}} d\theta\int_b^c\left(\sqrt{p^2 - r^2} - \frac{\delta}{2}\right)rdr\\ &= \int_a^{\frac{\pi}{4}}\left[-\frac{1}{3}(p^2 - r^2)^{\frac{3}{2}} - \frac{\delta}{4}r^2\right]\Bigg|_b^c d\theta\\ &= \int_a^{\frac{\pi}{4}}\left[-\frac{\delta^3}{24} + \frac{1}{3}(p^2 - b^2)^{\frac{3}{2}} - \frac{\delta}{4}c^2 + \frac{1}{16}\frac{\delta^3}{(\sin\theta)^2}\right]d\theta\end{aligned}$$

, in which $a = \arctan\frac{\frac{\delta}{2}}{\sqrt{p^2 - 2\left(\frac{\delta}{2}\right)^2}}$, $c = \sqrt{p^2 - \left(\frac{\delta}{2}\right)^2}$, and $b = \frac{\delta}{2\sin\theta}$.

C The Derivation of Eq. (11)

We accomplish this proof by studying the difference between $\frac{A(m)}{B(m)}$ and $\frac{1}{2}$. First, we see

$$\begin{aligned}A(m)-\frac{B(m)}{2} &= 8\sum_{i=2}^{l}(i-1)^2\arctan\frac{\sqrt{8(i-1)^2-\theta_{m+1}^2}}{\theta_{m+1}}-4\sum_{i=2}^{l}\theta_{m+1}\sqrt{2(i-1)^2-\theta_{m+1}^2}+2\sum_{i=2}^{l}\theta_m\sqrt{2(i-1)^2-\theta_m^2}\\&+\sum_{i=2}^{l}\sqrt{2(i-1)^2-\frac{1}{4}}-4\sum_{i=2}^{l}(i-1)^2\arctan\frac{\sqrt{8(i-1)^2-\theta_m^2}}{\theta_m}-4\sum_{i=2}^{l}(i-1)^2\arctan\sqrt{8(i-1)^2-1}\end{aligned} \tag{19}$$

When $l\to\infty$, we have the following approximations:

$$\begin{aligned}&\sum_{i=2}^{l}\sqrt{2(i-1)^2-\frac{1}{4}}\longrightarrow\sum_{i=2}^{l}\sqrt{2}(i-1),\qquad \sum_{i=2}^{l}\theta_{m+1}\sqrt{2(i-1)^2-\theta_{m+1}^2}\longrightarrow\sum_{i=2}^{l}\theta_{m+1}\sqrt{2}(i-1)\\&\sum_{i=2}^{l}\theta_m\sqrt{2(i-1)^2-\theta_m^2}\longrightarrow\sum_{i=2}^{l}\theta_m\sqrt{2}(i-1),\qquad \sum_{i=2}^{l}(i-1)^2\arctan\frac{\sqrt{8(i-1)^2-\theta_{m+1}^2}}{\theta_{m+1}}\longrightarrow\sum_{i=2}^{l}(i-1)^2\arctan 2\sqrt{2}(i-1)\\&\sum_{i=2}^{l}(i-1)^2\arctan\frac{\sqrt{8(i-1)^2-\theta_m^2}}{\theta_m}\longrightarrow\sum_{i=2}^{l}(i-1)^2\arctan 2\sqrt{2}(i-1)\\&\sum_{i=2}^{l}(i-1)^2\arctan\sqrt{8(i-1)^2-1}\longrightarrow\sum_{i=2}^{l}(i-1)^2\arctan 2\sqrt{2}(i-1)\end{aligned} \tag{20}$$

Plugging the left-hand side of six formulae in (20) into Eq. (19), we get $A(m)-\frac{B(m)}{2}\longrightarrow 0$ and thus $A(m)\longrightarrow\frac{B(m)}{2}$.

D Proof of Theorem 2

Proof Proof is accomplished in a similar way to that of Theorem 1. We have $\dfrac{\alpha(m+1,s)}{\alpha(m,s)}=\dfrac{A(m,s)}{B(m,s)}$ where

$$\begin{aligned}A(m,s) &= 1+\frac{4\sqrt{2}(l+l^2)}{s^{1+m}}-l\left(1-\frac{2}{s^{1+m}}\right)^2+4(l-1)\left(\frac{1}{2}-\frac{1}{s^{1+m}}\right)^2-4\sum_{i=2}^{l}\theta'_{m+1}\sqrt{2(i-1)^2-{\theta'_{m+1}}^2}\\&+8\sum_{i=2}^{l}(i-1)^2\arctan\frac{\sqrt{2(i-1)^2-{\theta'_{m+1}}^2}}{\theta'_{m+1}}+\sum_{i=2}^{l}\sqrt{8(i-1)^2-1}-8\sum_{i=2}^{l}(i-1)^2\arctan\sqrt{8(i-1)^2-1}\ ,\end{aligned} \tag{21}$$

and

$$\begin{aligned}B(m,s) &= 1+\frac{4\sqrt{2}(l+l^2)}{s^{m}}-l\left(1-\frac{2}{s^{m}}\right)^2+4(l-1)\left(\frac{1}{2}-\frac{1}{s^{m}}\right)^2-4\sum_{i=2}^{l}\theta'_{m}\sqrt{2(i-1)^2-{\theta'_{m}}^2}\\&+8\sum_{i=2}^{l}(i-1)^2\arctan\frac{\sqrt{2(i-1)^2-{\theta'_{m}}^2}}{\theta'_{m}}+\sum_{i=2}^{l}\sqrt{8(i-1)^2-1}-8\sum_{i=2}^{l}(i-1)^2\arctan\sqrt{8(i-1)^2-1}\end{aligned} \tag{22}$$

As in Appendix C, by comparing the value of $\dfrac{A(m,s)}{B(m,s)}$ to $\dfrac{1}{s}$, we get

$$\begin{aligned}A(m,s)s-B(m,s) &= (s-1)\sum_{i=2}^{l}\sqrt{8(i-1)^2-1}-8(1-s)\sum_{i=2}^{l}(i-1)^2\arctan\sqrt{8(i-1)^2-1}\\&-4(1-s)\sum_{i=2}^{l}\theta'_{m+1}\sqrt{2(i-1)^2-{\theta'_{m+1}}^2}+8(s-1)\sum_{i=2}^{l}(i-1)^2\arctan\frac{\sqrt{2(i-1)^2-{\theta'_{m+1}}^2}}{\theta'_{m+1}}\end{aligned} \tag{23}$$

When $l\to\infty$, we have the following approximations.

$$\begin{aligned}&\sum_{i=2}^{l}\sqrt{2(i-1)^2-{\theta'_{m+1}}^2}\longrightarrow\frac{1}{2}\sum_{i=2}^{l}\sqrt{8(i-1)^2-1}\ ,\\&\sum_{i=2}^{l}(i-1)^2\arctan\frac{\sqrt{8(i-1)^2-{\theta'_{m+1}}^2}}{\theta'_{m+1}}\longrightarrow\sum_{i=2}^{l}(i-1)^2\arctan\sqrt{8(i-1)^2-1}\end{aligned} \tag{24}$$

Plugging the left-hand side of the above two formulae into Eq. (23), we get $sA(m,s)-B(m,s)\longrightarrow 0$ and this concludes the proof.

E Quantities Related to Theorem 4

For easy presentation, we denote $x = r/\delta$. The maximal bucket region for the first bucket is

$$g(1) = \pi q^2 + 4q\delta + \delta^2$$

and that for the second bucket is

$$g(2) = \left\{\pi(\sqrt{2}+x)^2 + 4(\sqrt{2}+x) + 1 - 8\left[\left(\arctan\sqrt{7} - \frac{\pi}{4}\right) - \frac{1}{8}(\sqrt{7}-1)\right]\right\}\delta^2$$

The coverable region for bucket 1 is

$$f(1,m) = \left[2\pi + 4\sqrt{2}\left(1 - \frac{2}{2^m}\right) - \frac{4}{2^m} + \frac{4}{2^{2m}} + 1\right]\delta^2$$

and that for bucket 2 is

$$f(2,m) = \left\{\pi(\sqrt{2}+x)^2 + 4(\sqrt{2}+x)\left(1 - \frac{2}{2^m}\right) - \frac{4}{2^m} + \frac{4}{2^{2m}} + 1 - 8\left\{\left[\arctan\frac{\sqrt{2-\theta_m^2}}{\theta_m} - \frac{\pi}{4}\right] - \frac{1}{2}\left[\sqrt{2-\theta_m^2} - \theta_m\right]\theta_m\right\}\right\}\delta^2$$

Therefore, we have $\frac{\alpha(m+1)}{\alpha(m)} = \frac{A(m)}{B(m)}$ where

$$A(m) = 4(2\sqrt{2}+x)\frac{2}{2^{m+1}} + \frac{8}{2^{m+1}} - \frac{8}{2^{2m+2}} + \sqrt{7} - 1 - 8\arctan\sqrt{7} + 8\arctan\frac{\sqrt{2-\theta_{m+1}^2}}{\theta_{m+1}} - 4\left[\sqrt{2-\theta_{m+1}^2} - \theta_{m+1}\right]\theta_{m+1}$$

and

$$B(m) = 4(2\sqrt{2}+x)\frac{2}{2^{m}} + \frac{8}{2^{m}} - \frac{8}{2^{2m}} + \sqrt{7} - 1 - 8\arctan\sqrt{7} + 8\arctan\frac{\sqrt{2-\theta_{m}^2}}{\theta_{m}} - 4\left[\sqrt{2-\theta_{m}^2} - \theta_{m}\right]\theta_{m}$$

In a straightforward way, the above can give rise to the following.

$$A(m) \leq \frac{1}{2}B(m)$$